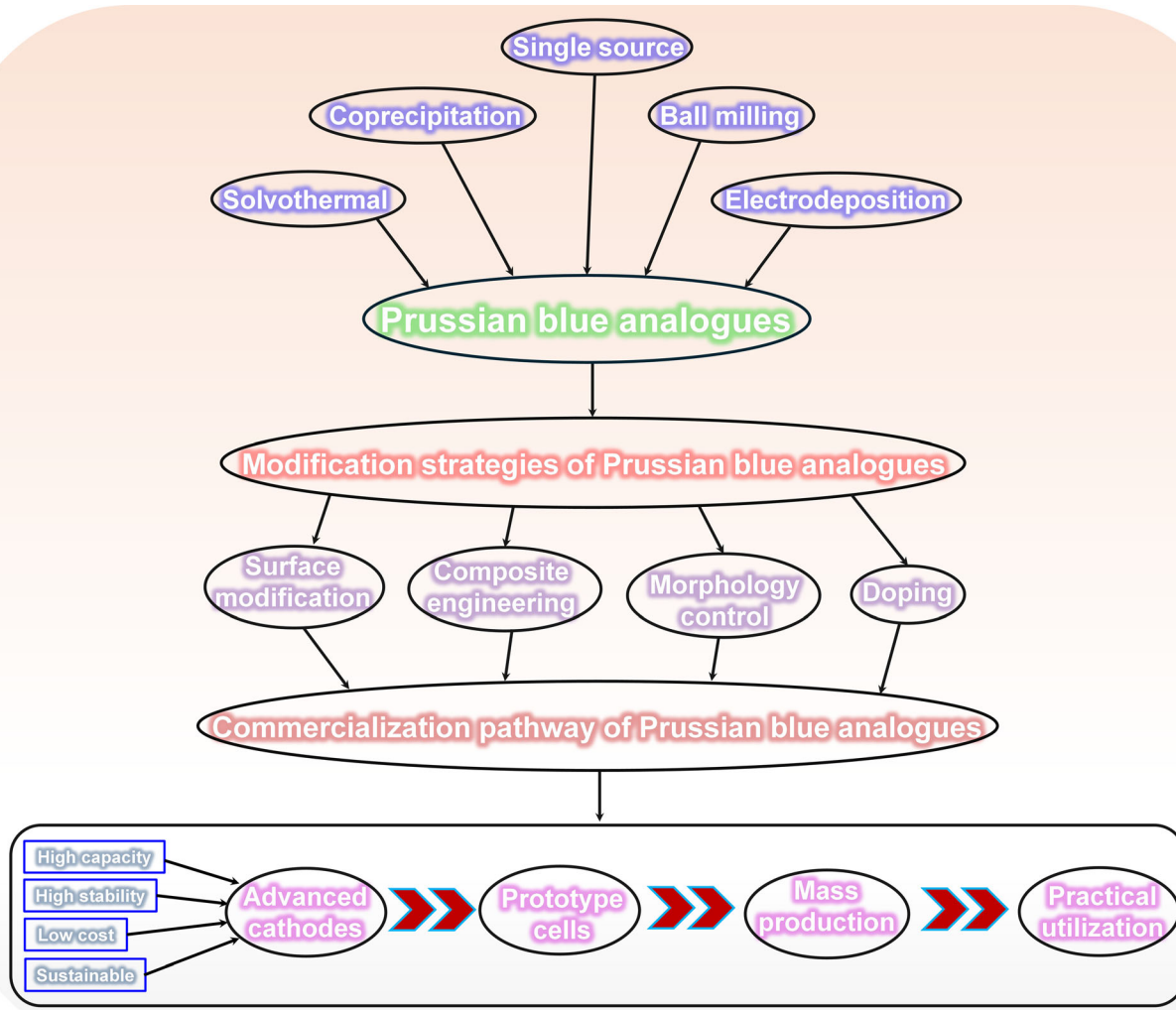


# Prussian Blue Analogs as Cathode Materials for Sodium-Ion Batteries

Narasimharao Kitchamsetti,\* Ana L. F. de Barros, and Sungwook Mhin\*



Prussian blue analogs (PBAs) have shown great promise as cathode materials for sodium-ion batteries (SIBs) due to their easy synthesis, affordability, structural adaptability, and high theoretical capacity. However, despite their considerable potential, there are still several performance challenges that hinder their practical use. This review thoroughly explores the structures of PBAs and their electrochemical reaction mechanisms, systematically summarizing current synthesis methods and modification techniques

while providing forward-looking insights. Additionally, the industrial viability of PBAs is assessed from a commercialization standpoint. By examining advanced synthesis methods, material optimization strategies, and challenges in industrial development, this work aims to provide both theoretical guidance and technical prospects for enhancing the application of PBAs in practical SIBs.

## 1. Introduction

The finite supply of fossil fuels and their extensive use over the years have resulted in significant environmental pollution, prompting researchers to investigate cleaner and more sustainable energy alternatives like solar, wind, and hydropower.<sup>[1,2]</sup> To enhance the efficiency of renewable energy use and facilitate effective energy conversion, there is an increasing need for advanced electrochemical energy storage systems, which encompass different kinds of supercapacitors and metal-ion batteries.<sup>[3–5]</sup>

Lithium-ion batteries (LIBs) have become the leading energy storage solution for portable electronics and electric vehicles, thanks to their high specific capacity, long lifespan, and excellent Coulombic efficiency.<sup>[6]</sup> However, their widespread use faces several significant challenges. First, global lithium (Li) reserves are finite, and the extensive use of LIBs could result in resource shortages. Second, the flammability of organic electrolytes and the potential for Li dendrite formation pose safety risks.<sup>[7,8]</sup> Third, LIB performance tends to decline significantly in low-temperature and high-demand conditions, which limits their application in large-scale energy storage systems. In contrast, new metal-ion batteries show greater promise for large-scale energy storage.<sup>[9]</sup> Alternative charge carriers like K<sup>+</sup>, Na<sup>+</sup>, Ca<sup>2+</sup>, Mg<sup>2+</sup>, and Al<sup>3+</sup> can help mitigate the resource limitations associated with Li.<sup>[10–12]</sup> Among these options, sodium-ion batteries (SIBs) have attracted considerable research interest due to the abundance of sodium (Na) reserves, lower costs, and superior performance in low-temperature conditions.

It is important to note that SIBs can take advantage of cost-effective and lightweight aluminum (Al) as current collectors on both the cathode and anode sides. This benefit arises from Na's

inability to form alloys with Al at low potentials, which significantly lowers raw material expenses.<sup>[13,14]</sup> Additionally, Al's high oxidation potential enables SIBs to be discharged to 0 V during storage and transport without greatly affecting their electrochemical performance, thus improving battery safety.<sup>[15]</sup> In contrast, the lattice octahedral void size of metallic Al is similar to that of Li, making it easy to create intermetallic compounds with Li. As a result, Cu must be used as the current collector for LIB anodes, and the cell voltage must be kept above 2 V to avoid Cu oxidation or dissolution at low potentials, which could increase the risk of internal short circuits.<sup>[16]</sup> In terms of kinetic performance, SIBs have significant advantages. Sodium (Na<sup>+</sup>) ions have a smaller solvation radius, lower solvation energy, and weaker charge density compared to lithium ions (Li<sup>+</sup>), which together facilitate faster ion migration and improved ion diffusion at the electrolyte-electrode interfaces.<sup>[17,18]</sup> Experimental findings indicate that Na-based electrolytes exhibit higher ionic conductivity than Li-based systems at the same concentrations, or similar conductivity at lower concentrations. This property allows SIBs to achieve quicker charging rates while minimizing reliance on high-concentration electrolytes.<sup>[19,20]</sup>

The progress of SIBs heavily relies on the creation of high-performance cathode materials, which are crucial for their technological advancement. An ideal cathode material for SIBs should have several key attributes: a high redox potential, significant gravimetric specific capacity, excellent structural stability, and good electronic conductivity.<sup>[21]</sup> These characteristics work together to improve energy density, extend cycle life, and ensure the efficient and stable functioning of SIBs. Additionally, it is important to design cathode materials that are safe, nontoxic, affordable, and suitable for large-scale production to lower the overall cost of SIBs, enhancing their competitiveness as a practical alternative to LIBs in energy storage. So far, researchers have created a variety of cathode material systems for SIBs, mainly including layered transition metal oxides (TMOs),<sup>[22,23]</sup> Prussian blue analogs (PBAs),<sup>[24,25]</sup> organic compounds (OEMs),<sup>[26,27]</sup> and polyanionic compounds (PACs).<sup>[28–30]</sup> The electrochemical performance of different cathode materials is illustrated in Figure 1.

Among these, PBAs offer several notable benefits: (1) Their 3D open framework design includes stable and rigid diffusion channels, which facilitate efficient Na ion transport and excellent cycling stability. (2) The availability of abundant raw materials, straightforward synthesis methods, and low costs give PBAs significant potential for large-scale energy storage applications. (3) The presence of numerous redox-active sites, along with

N. Kitchamsetti  
National & Local United Engineering Laboratory for Power Batteries  
Faculty of Chemistry  
Northeast Normal University  
Changchun 130024, P. R. China  
E-mail: nrkn123@nenu.edu.cn

A. L. F. de Barros  
Laboratory of Experimental and Applied Physics  
Centro Federal de Educação Tecnológica Celso Suckow da Fonseca  
Av. Maracanã Campus, 229, Rio de Janeiro 20271-110, Brazil

S. Mhin  
Department of Energy and Materials Engineering  
Dongguk University  
Seoul 04620, Republic of Korea  
E-mail: swmhin@dongguk.edu

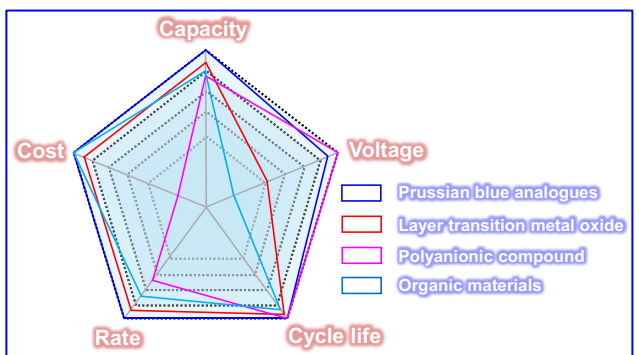


Figure 1. Schematic diagram of the advantages and disadvantages of cathode materials for SIBs.

highly reversible phase transition behavior, works together to improve charge storage capacity and reaction kinetics.<sup>[31–33]</sup> These features make PBAs a strong candidate for cathode materials in the advancement of SIBs. This review highlights recent progress in the use of PBAs as cathodes for SIBs, discussing their structural properties, synthesis techniques, and modification approaches, with the goal of offering new insights and perspectives for the further development of PBAs (Figure 2).

## 2. Crystal Structure of PBAs

PBAs are defined by the general chemical formula  $A_xM[R(CN)_6]_zH_2O$ , where A signifies mobile carrier ions (such as  $Li^+$ ,  $Na^+$ ,  $K^+$ ,  $NH_4^+$ ,  $H^+$ ,  $Zn^{2+}$ ,  $Al^{3+}$ ) with a stoichiometric coefficient x typically between 0 and 2, indicating how many A sites are occupied.<sup>[34]</sup> Both M (like Fe, Cu, Ni, Co, Mn, V, Zn) and R (such as Fe, Cu, Ni, Co) are transition metals (TMs). The valence changes of M and R during electrochemical charge and discharge processes enhance the material's charge storage capacity.<sup>[35,36]</sup> As illustrated in Figure 3a, M ions bond with nitrogen (N) atoms from cyanide

ligands to create  $[MN_6]$  octahedra, which usually have high-spin electron configurations, while R ions bond with carbon (C) atoms to form  $[RC_6]$  octahedra, primarily in low-spin states.<sup>[37–39]</sup> The difference in spin states arises from the distinct electronic properties of the N and C ligands. Nitrogen, being more electronegative and having a higher electron-donating ability compared to carbon, creates a stronger ligand field. This stronger ligand field leads to a greater splitting of the d-orbitals of the TM ions. As a result, the higher-energy d-orbitals are more stabilized, and this stabilizing effect is often associated with a high-spin configuration for metals such as Fe, Co, and Mn. On the other hand, carbon, being less electronegative and a weaker electron-donating ligand, produces a weaker ligand field. This results in a smaller splitting of the d-orbitals, favoring low-spin configurations for TM ions. The low-spin states typically correspond to lower-energy electronic configurations, particularly in metal centers with higher oxidation states. These two types of octahedra are arranged alternately through corner-sharing, forming a 3D open framework with large interstitial spaces for guest ions. The parameter z indicates the number of water molecules in the lattice. The bond lengths of R–C and M–N directly influence the lattice constants of PBAs, which can affect ion migration rates and overall electrochemical performance. During cycling, the reversible insertion and extraction of guest ions, along with associated redox reactions, lead to dynamic adjustments in the lattice parameters. However, these structural changes are highly reversible, contributing to the excellent cycling stability of PBAs as electrode materials.<sup>[40–42]</sup>

TM elements R and M have specific functions in PBAs. The ions at the  $R_{site}$  are crucial for determining the electrochemical characteristics of the material, especially their redox potentials.<sup>[43]</sup> For example, when R is Cr or Mn, PBAs show redox potentials of  $\approx -0.8$  and 0 V (versus SHE), respectively. This indicates greater stability and more negative operating voltages, making them more appropriate as anode materials for nonaqueous battery systems rather than as cathodes for SIBs.<sup>[44,45]</sup> On the other hand, Fe-based PBAs (where R = Fe) have higher redox potentials



**Narasimharao Kitchamsetti** received his Ph.D. degree from Indian Institute of Technology Indore, India, in 2021. He is now a teacher at Northeast Normal University, PR China. His current research focuses on design of advanced functional materials for supercapacitors, and rechargeable batteries.



**Ana L. F. de Barros** received her Ph.D. from the Department of Physics, Federal University of Rio de Janeiro, Brazil, in 2004. She then worked as a Postdoctoral Researcher at the Queen's University of Belfast, QUB, Northern Ireland, UK. She is presently working as a Professor in the Department of Physics at the Centro Federal Center for Technological Education of Rio de Janeiro, Brazil. Her research interests include atomic and molecular physics, nanotechnology, energy storage, and photocatalytic water treatment applications.



**Sungwook Mhin** is a professor in the Department of Energy and Materials Engineering at Dongguk University, South Korea. Dr. Mhin earned his B.S. and M.S. degrees from Hanyang University and received his Ph.D. from the University of Florida. His work centers on the development of advanced functional materials for water electrolysis, triboelectric and piezoelectric energy harvesting, and next-generation secondary batteries such as lithium-ion and aqueous zinc-ion batteries.

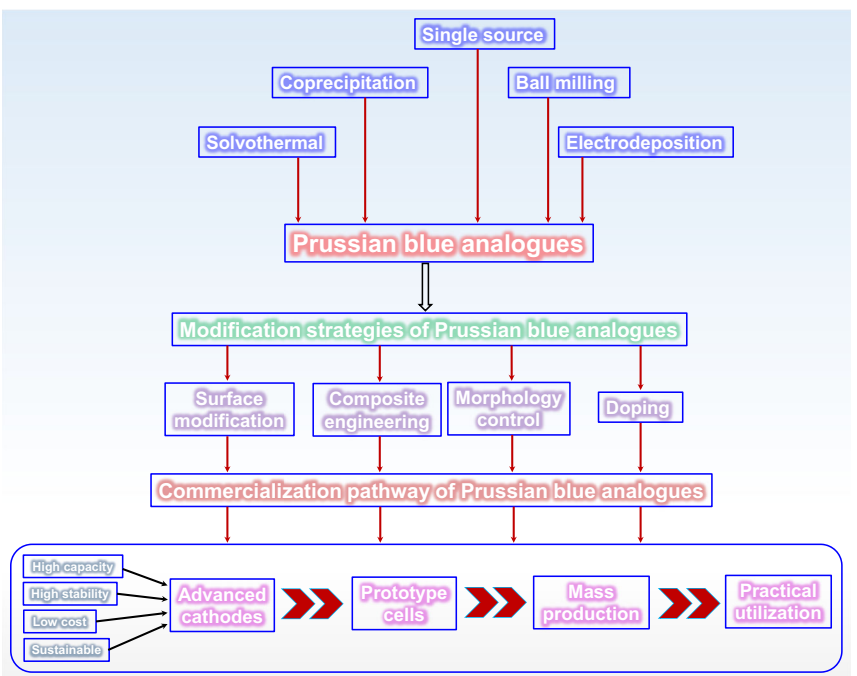


Figure 2. Summary of the preparation methods, advanced modification strategies, and application prospect of PBAs for SIBs.

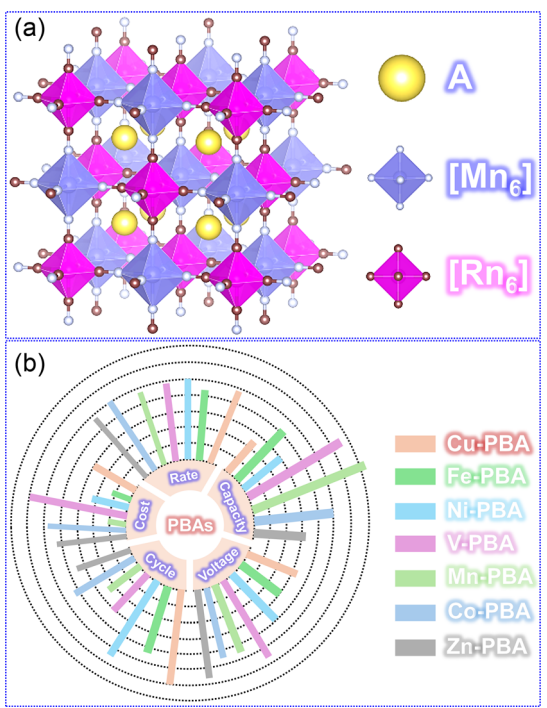


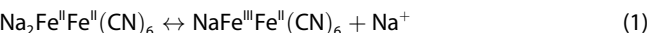
Figure 3. a) The structure of PBAs, and b) the characteristics of different PBAs.

(around 1 V versus SHE), which places them within the electrochemical stability range of water, making them excellent candidates for SIB cathodes.<sup>[46,47]</sup> The range of M-site ions is more extensive. Although substitutions at the M site usually do not significantly change the crystal structure of PBAs, larger cation radii

at the M site result in increased lattice parameters. Common metals found at the M site include Cu, Fe, Ni, Mn, V, and Co.<sup>[47,48]</sup> As illustrated in Figure 3b, PBAs with varying M-site compositions show significant differences in electrochemical performance. While both V-PBAs and Mn-PBAs exhibit high specific capacities, the high cost of V limits its practical use. In comparison, V-PBAs and Zn-PBAs have relatively higher average working voltages, while Ni-PBAs and Cu-PBAs offer better cycling stability. However, it is important to note that Ni-PBAs, Cu-PBAs, and Zn-PBAs generally have lower specific capacities. Notably, all PBAs show excellent rate capability.<sup>[49–51]</sup>

### 3. The Reaction Mechanisms of PBAs

A comprehensive grasp of the reaction mechanisms that control the (de)intercalation of guest cations in PBAs is essential for creating high-performance electrode materials for SIBs. PBAs can be classified into two categories based on their redox properties: single-electron transfer types, which have a theoretical capacity of approximately 85 mAh g<sup>-1</sup>, and double-electron transfer types, with a theoretical capacity of around 170 mAh g<sup>-1</sup>.<sup>[52]</sup> For instance, the double-electron transfer material FeHCF follows a stepwise reaction mechanism that unfolds as follows



This process of transferring two electrons usually appears as two separate redox peaks in cyclic voltammetry (CV). The

separation between these peaks is caused by variations in the coordination environments of TMs. Low-spin metal sites display higher redox potential due to the influence of strong ligand fields, whereas high-spin sites have lower potentials because of weaker ligand fields (**Figure 4a,b**).

It is important to note that materials such as Mn-HCF can exhibit single redox peaks when the redox potentials of  $\text{Fe}^{2+}/\text{Fe}^{3+}$  and  $\text{Mn}^{2+}/\text{Mn}^{3+}$  align. However, this balance is affected by the presence of interstitial water molecules, which can cause the redox peaks to separate by diminishing the effects of the ligand field. Additionally, dual-active-site PBAs typically experience more significant changes in lattice volume during cycling, and this structural stress can lead to faster material degradation, ultimately affecting the long-term stability of the electrode during cycling.<sup>[52]</sup>

To understand the  $\text{Na}^+$  transport mechanisms in PBAs, it is important to examine their diffusion pathways and site-occupancy kinetics. When paired with density functional theory (DFT) calculations, advanced *in situ*/operando characterization techniques help to uncover the relationships between metal-ion site occupancy and  $\text{Na}^+$  diffusion pathways. Peng et al.<sup>[44]</sup> successfully produced high-quality ternary  $\text{Ni}_x\text{Co}_{1-x}[\text{Fe}(\text{CN})_6]$  PBAs using a cocrystallization method involving a chelator and surfactant. The introduction of inert Ni ions effectively reduced capacity

loss caused by excessive lattice distortion, allowing for better control over charge and discharge depth. DFT calculations further elucidated the  $\text{Na}^+$  transport mechanisms in PBAs as shown in Figure 4c;  $\text{Na}^+$  can occupy four interstitial sites (8c, 24d, 32f(n), 32f(c)), with 8c providing the most space and 24d having the lowest binding energy ( $E_b$ ), indicating that 24d is the most thermodynamically stable  $\text{Na}^+$  site in Fe-based PBAs. In the cubic PBA structure,  $\text{Na}^+$  diffusion occurs through two main pathways: the S-shaped path and the axial path (Figure 4d,e). Energy barrier calculations indicated that the S-path has a lower activation energy ( $E_a$ ), making it more favorable kinetically. Importantly, the presence of numerous 24d sites in PBAs not only facilitates a 3D distribution of  $\text{Na}^+$  but also lowers  $E_a$  through cooperative motion of multiple ions. This efficient  $\text{Na}^+$  transport mechanism significantly improves the rate capability of SIB cathodes.

## 4. Preparation Methods

### 4.1. Coprecipitation

The coprecipitation method is the oldest and most commonly used technique for producing PBAs, offering benefits such as low

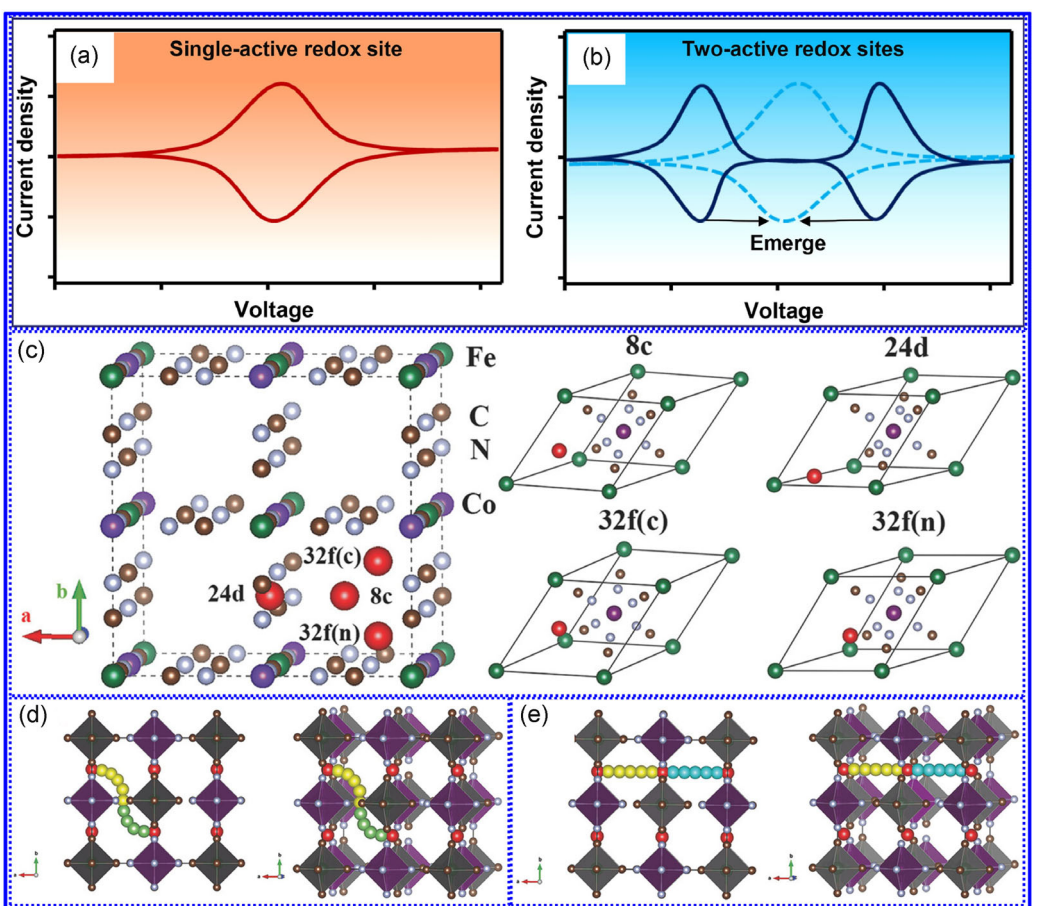


**Figure 4.** a,b) Schematic CV plots for the PB/PBAs with single- and two-active redox sites. Adapted with permission.<sup>[52]</sup> Copyright 2022, Elsevier B.V. c) The typical crystal structure of an A-free HCF ( $\text{Fe}_4[\text{Fe}(\text{CN})_6]_3$ ) with possible interstitial positions (in red). The front views and corresponding side views of  $\text{Na}^+$  migration of d) S-shaped path and e) axial path. Adapted with permission.<sup>[44]</sup> Copyright 2018, Wiley-VCH.

cost, straightforward processing, no need for high-temperature treatments, and excellent scalability.<sup>[53–55]</sup> This method generally involves combining metal-ion salts with cyanide-containing ligands in a solution while carefully managing reaction conditions like pH and temperature to promote the coprecipitation of the desired product. Importantly, because of the very low solubility product constant ( $K_{sp} \approx 10^{-15}$ ) of  $\text{Na}_x\text{M}[\text{Fe}(\text{CN})_6]$ , the processes of nucleation and growth happen almost at the same time, resulting in the creation of many VFe(CN) vacancies and  $\text{H}_2\text{O}$  molecules within the structure.<sup>[56,57]</sup> As a result, irregularly shaped and randomly clustered nanoparticles (NPs) of about 50 nm are produced (Figure 5a,b). To obtain a more uniform morphology, researchers have investigated various methods, including adjusting pH, controlling aging time, regulating solution mixing rates, and managing temperature precisely.<sup>[58,59]</sup>

The use of chelating agents has notably improved the crystallinity of PBAs. Citrate, a commonly used chelating agent, serves two important functions in the synthesis of PBAs. First, it binds with metal ions, which help to slow down rapid nucleation and significantly decrease nucleation kinetics.<sup>[60,61]</sup> This reduction in uncontrolled crystal aggregation leads to the development of PBAs with better quality and enhanced crystallinity. Second, during the synthesis process, citrate salts (such as sodium citrate or potassium citrate) create an environment that is rich in guest ions.

This ion-rich environment promotes the incorporation of a greater concentration of guest ions into the PBAs structure, which stabilizes the framework and minimizes the formation of vacancies and crystalline water.

For example, Wu et al.<sup>[62]</sup> created a citrate-assisted controlled crystallization technique that effectively produced highly crystalline, low-defect  $\text{Na}_2\text{CoFe}(\text{CN})_6$  nanocrystals. As shown in Figure 5c,d, citrate aids in the development of well-defined cubic structures of Prussian blue (PB). Shen et al.<sup>[63]</sup> introduced a synergistic method that utilized polyvinylpyrrolidone (PVP) as a surfactant and sodium citrate as a chelating agent, which created a  $\text{Na}^+$ -rich microenvironment. This optimized coprecipitation technique allowed them to successfully synthesize highly stable monoclinic  $\text{Na}$ -enriched Ni hexacyanoferrate ( $m\text{-NiHCF}$ ) nanocubes (NCs) with a well-defined shape. To enhance this method, Qin et al.<sup>[64]</sup> conducted a thorough study on the chelation mechanism of citrate. They suggested a chemically inhibited strategy that leveraged the combined effects of  $\text{H}^+$  and citrate. By adjusting the concentration of sodium citrate, they were able to achieve tunable crystallinity in PBAs, showcasing precise control over the structural properties of the material.

However, when citrate is used as a chelating agent, it fails to adequately eliminate vacancies, resulting in a significant presence of VFeCN defects within the PBAs crystal structure. This

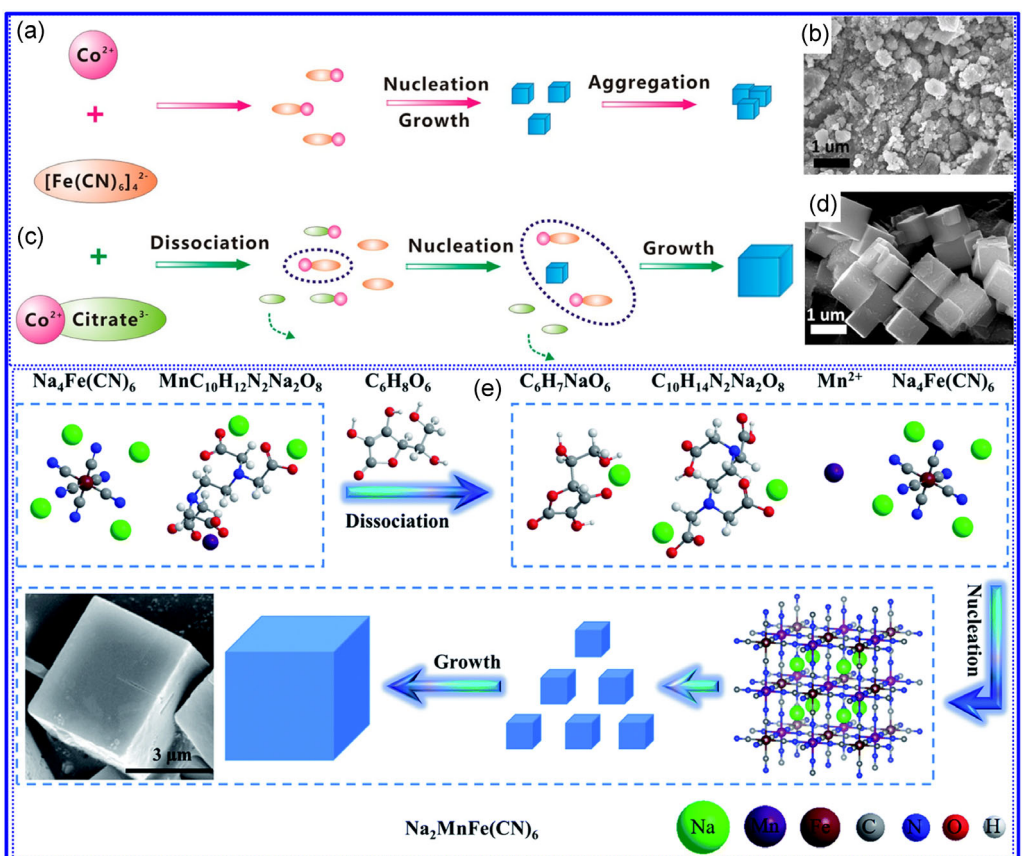


**Figure 5.** Schematic illustration of the a,b) conventional coprecipitation process and c,d) the citrate-assisted controlled crystallization process for the synthesis of  $\text{Na}_2\text{CoFe}(\text{CN})_6$ . Adapted with permission.<sup>[62]</sup> Copyright 2016, American Chemical Society. e) Schematic illustration of the synthesis procedure of highly crystalline Prussian white  $\text{Na}_{1.92}\text{Mn}[\text{Fe}(\text{CN})_6]_{0.98}$  microcube crystals. Adapted with permission.<sup>[65]</sup> Copyright 2019, Royal Society of Chemistry.

leads to poor rate capability and cycling stability. To effectively control crystallization, high concentrations of citrate are necessary (for instance, a molar ratio of  $\text{Na}_3\text{Cit}$  to  $\text{Na}_4\text{Fe}(\text{CN})_6$  greater than 5:1), which raises production costs and environmental issues. To decrease VFeCN levels while enhancing environmental sustainability and cost efficiency, stronger chelating agents like disodium ethylenediaminetetraacetate ( $\text{Na}_2\text{EDTA}$ ) can be effective alternatives to citrate. The superior chelation ability of EDTA derivatives allows for better vacancy suppression at lower concentrations. As shown in Figure 5e, Peng et al.<sup>[65]</sup> successfully created highly crystalline Mn-based PBA (H-PBM) using EDTA- $\text{MnNa}_2$  chelate and  $\text{Na}_4[\text{Fe}(\text{CN})_6]$  as precursors through carefully controlled crystal growth. A crucial element of this synthetic approach is the strong chelation effect of EDTA on  $\text{Mn}^{2+}$ , which enables the controlled release of  $\text{Mn}^{2+}$  from the  $[\text{EDTA}-\text{Mn}]^{2-}$  complex by adding the right amount of weak acid to manage the crystallization process. Characterization results indicate that the resulting H-PBM particles have an ideal cubic shape, significantly fewer defects, and high Na content.

Shang et al.<sup>[66]</sup> further enhanced the content of EDTA- $\text{MnNa}_2$  to take advantage of its strong ability to chelate  $\text{Mn}^{2+}$ , which led to the formation of unconventional cationic Mn vacancies (VMn) on the surface of the Mn-Fe PBA. This method effectively reduced the motion of the Mn-N bond and mitigated the Jahn-Teller effect, resulting in significantly improved stability. Additionally, Wang et al.<sup>[67]</sup> introduced ascorbic acid to temper the overly strong chelating ability of  $\text{Na}_2\text{EDTA}$  toward  $\text{Mn}^{2+}$ , successfully creating EDTA-1MVC with multielement doping (Fe, Co, Cu, Mn, Ni), thus broadening the application potential of  $\text{Na}_2\text{EDTA}$ . Moreover, Jiang et al.<sup>[68]</sup> successfully used Na carboxymethyl cellulose (CMC) as a chelating agent to produce low-defect PB (LD-PB). In comparison to citrate and EDTA, CMC's moderate binding strength with metal ions is more effective in minimizing both defects and the content of crystalline water.

## 4.2. Single Source

The single source method offers a more advanced technique compared to conventional coprecipitation. This method uses only a  $\text{Na}_4[\text{Fe}(\text{CN})_6]$  solution as the only source of Fe, removing the requirement for other Fe-containing substances. When certain reaction conditions are met,  $[\text{Fe}(\text{CN})_6]^{4-}$  breaks down to release  $\text{Fe}^{2+}$  ions. Because  $\text{Fe}^{2+}$  is easily oxidized, the reaction system sustains a mixed valence state of  $\text{Fe}^{2+}/\text{Fe}^{3+}$ . These Fe ions then react with the remaining  $[\text{Fe}(\text{CN})_6]^{4-}$  to produce PBA precipitates.

In 2014, Guo et al.<sup>[69]</sup> introduced an improved single source synthesis method. They started with a 0.02 m  $\text{Na}_4[\text{Fe}(\text{CN})_6]$  solution as the only Fe precursor and added a small amount of hydrochloric acid (HCl) at 60 °C, successfully creating high-quality  $\text{Na}_{0.61}\text{Fe}[\text{Fe}(\text{CN})_6]_{0.94}$  NCs. Later, they conducted the process at 80 °C in a  $\text{N}_2$  atmosphere with ascorbic acid, which effectively inhibited the oxidation of  $\text{Fe}^{2+}/[\text{Fe}^{3+}(\text{CN})_6]^{4-}$ , resulting in a product with a high Na content,  $\text{Na}_{1.63}\text{Fe}_{1.89}(\text{CN})_6$ . Additionally, Goodenough et al.<sup>[70]</sup> successfully synthesized rhombohedral R- $\text{Na}_{1.92}\text{Fe}[\text{Fe}(\text{CN})_6]$  using the single source method. This

technique provided significant benefits, leading to PBAs with notably higher Na content and very low crystalline water content. Building on this research, Wang et al.<sup>[71]</sup> further refined the single source synthesis, producing low-defect  $\text{Na}_{0.61}\text{Fe}_{1.94}(\text{CN})_6 \cdot 0.06$  (NaFe-PB) with a significantly reduced vacancy concentration (down to 0.06) and a well-defined cubic shape.

While the single-source technique allows for the creation of well-defined PBA crystals with lower levels of crystalline water and vacancy defects, it has notable drawbacks. The limited choice of precursors significantly restricts the ability to achieve precise stoichiometric control for elemental doping, and this method is currently restricted to Fe-Fe based PBAs. Additionally, the production of the highly toxic byproduct NaCN during the reaction poses serious safety risks, which greatly limits its feasibility for large-scale industrial use.

## 4.3. Solvothermal

The hydrothermal method is a synthesis technique that employs specially designed sealed reactors to create high-temperature and high-pressure conditions, allowing for the dissolution or recrystallization of substances that are typically insoluble at normal conditions.<sup>[72]</sup> In the synthesis of PBAs, this method offers three key benefits: (1) improved process control, as the ability to precisely adjust reaction temperature and pH allows for targeted regulation of material composition and structure; (2) enhanced morphological properties, with hydrothermally synthesized PBAs showing a uniform particle distribution and a significantly lower tendency to agglomerate; and (3) better structural integrity, as the resulting crystals feature long-range ordered lattice structures and clearly defined crystallographic planes.<sup>[73]</sup> Notably, this method allows for the controlled creation of various PBA architectures, from nanocrystals to complex hollow structures, by carefully managing nucleation and growth kinetics.<sup>[74]</sup>

To decrease the crystalline water content further, Wang et al.<sup>[75]</sup> developed a mixed solvent system combining water and ethylene glycol (EG) for creating monoclinic PB (M-PB). In this solvothermal synthesis, EG serves two main purposes: (1) its molecular steric hindrance prevents direct interaction between  $\text{Fe}^{2+}$  and  $[\text{Fe}(\text{CN})_6]^{4-}$ , effectively slowing down the crystal growth rate; (2) it acts as a mild reducing agent, preserving the valence stability of  $\text{Fe}^{2+}$  and avoiding structural defects caused by oxidation. This dual-regulation approach aids in forming M-PB with a stable lattice structure (Figure 6a). The research thoroughly examined how reaction time affects crystal morphology, showing that extending the reaction duration appropriately promotes the development of well-defined crystalline products (Figure 6b-d). Han et al.<sup>[76]</sup> successfully incorporated nitroso groups into PBAs through hydrothermal synthesis, resulting in highly stable Mn nitrosylpentacyanoferrate ( $\text{Mn}[\text{Fe}(\text{CN})_5\text{NO}]$ ) particles. The introduction of nitroso groups disrupts crystal symmetry, which helps mitigate the Jahn-Teller effect. Additionally, Zhang et al.<sup>[77]</sup> created an innovative machine learning model that systematically analyzes the relationship between architecture and activity across nine parameters during the hydrothermal synthesis of PBAs and

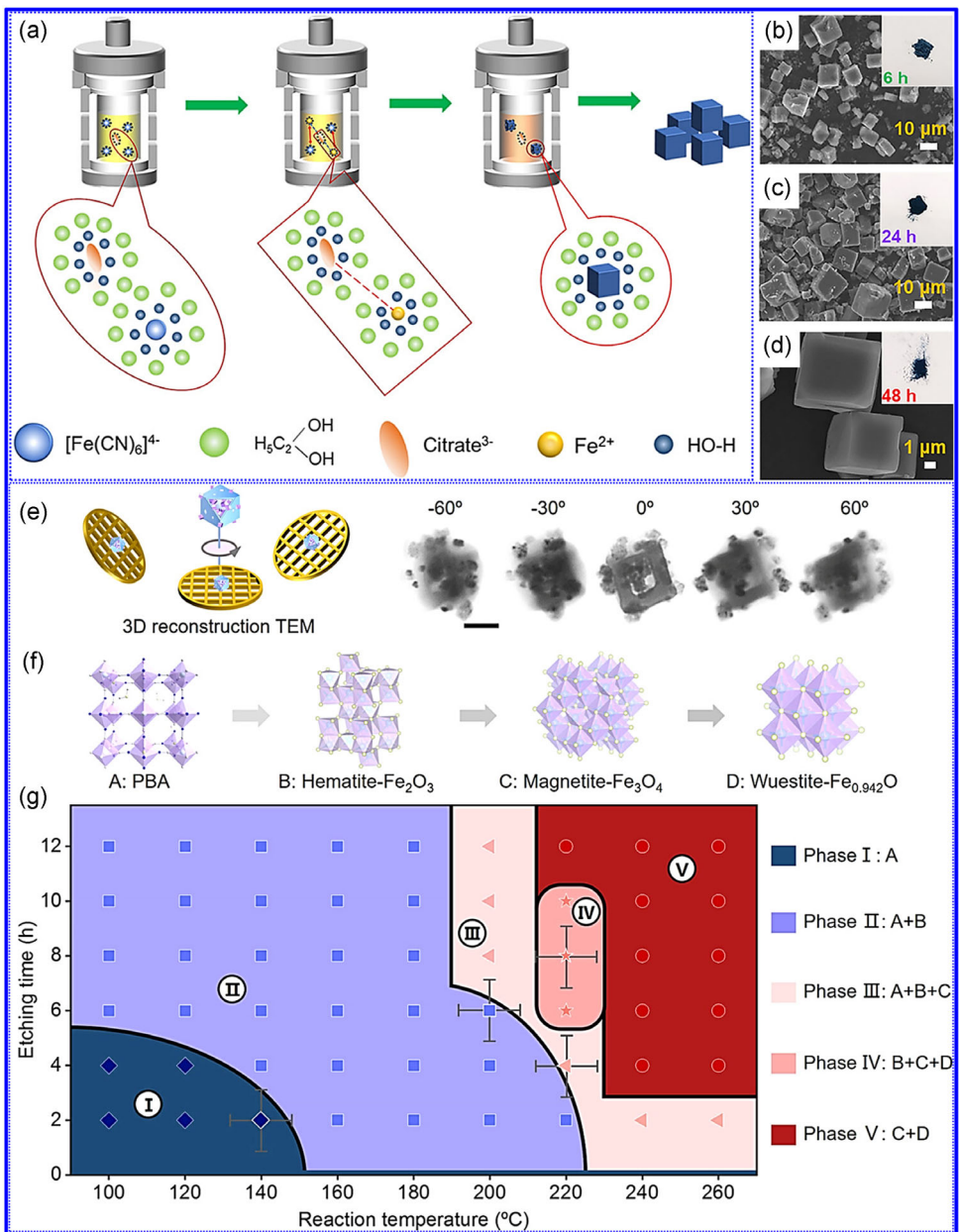


**Figure 6.** a) Schematic illustration of the preparation process of M-PB samples. b–d) SEM images of M-PB materials after various reaction time. Inset SEM images are digital images showing the color of the corresponding products. Adapted with permission.<sup>[75]</sup> Copyright 2022, American Chemical Society. e,f) 3D reconstructed TEM images of  $Fe_2O_3$ -NP@NiCoFePBA (scale bar, 100 nm) and crystal structure in the phase transition of PBA hydrothermal etching. g) Hydrothermal phase diagram of PBA. Adapted with permission.<sup>[77]</sup> Copyright 2024, American Chemical Society.

their derivatives, focusing on five key dimensions: synthesis conditions, phase transitions, atomic structure, crystal morphology, and electrochemical performance. This model enabled precise control over the synthesis of  $FeO_x$  NPs-modified PBAs (31 types of  $FeO_x$ -NP@PBAs) and established a hydrothermal phase diagram for the preparation of PB-based materials, serving as a universal framework for predicting structure-property relationships (Figure 6e-g). However, the hydrothermal method has limitations for widespread PBA synthesis due to its high equipment costs and low production yield, highlighting the need for solutions to enable scalable production.

#### 4.4. Ball Milling

Solvent-free mechanochemical synthesis, especially through the ball-milling technique, has become a popular method for preparing cathode materials. This approach has shown particular effectiveness in synthesizing PBAs. This promising and straightforward method for large-scale synthesis offers several distinct advantages, including (1) lower activation energy for reactions, (2) significantly improved molecular reactivity, (3) enhanced ion diffusion in solid state, and (4) the ability to facilitate chemical reactions at lower temperatures.

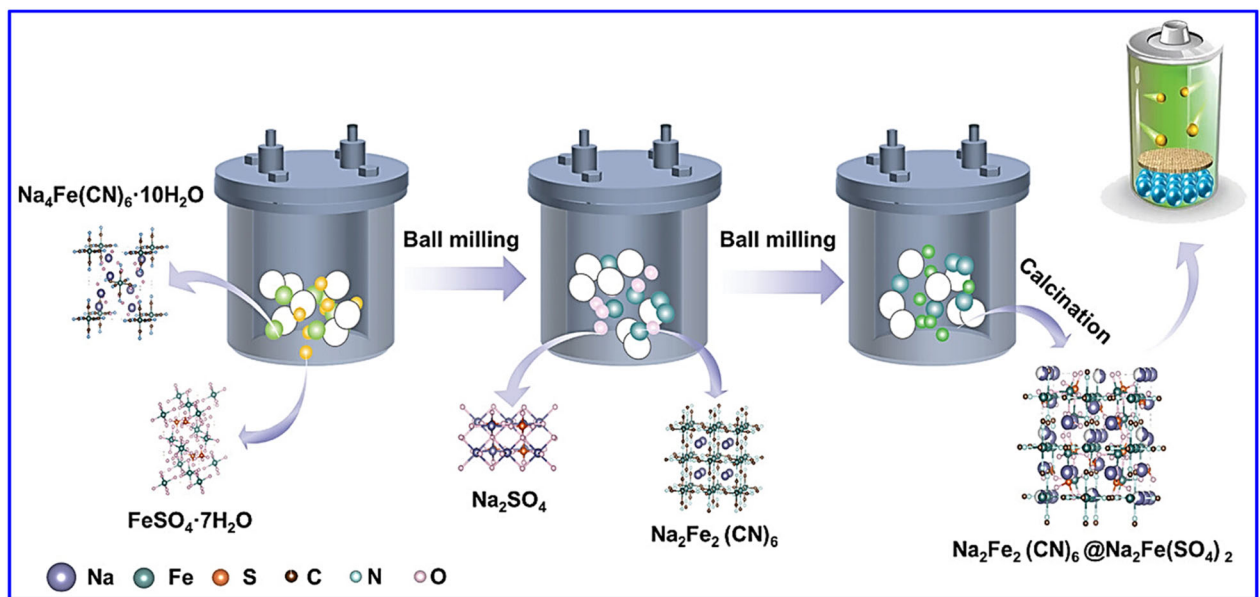


**Figure 7.** Schematic illustration of the ball milling process. Adapted with permission.<sup>[78]</sup> Copyright 2025, Wiley VCH.

In comparison to traditional coprecipitation methods, the ball milling technique provides benefits such as reduced processing time, lower reaction temperatures, and easier operational procedures.<sup>[78]</sup> Figure 7 illustrates the specific steps involved in the ball milling process.

The research conducted by Gong<sup>[79]</sup> and Tang<sup>[80]</sup> was groundbreaking in the successful synthesis of  $\text{NaFeFe}(\text{CN})_6$  material through low-energy mechanical ball milling. However, the resulting PBAs displayed a morphology characterized by particle agglomeration due to the creation of a thermodynamically unstable cubic phase structure, which resulted in less-than ideal electrochemical performance. To overcome this issue, He and colleagues<sup>[81]</sup> carefully regulated the crystalline water content in the precursor, successfully producing monoclinic  $\text{Na}_{1.94}\text{Mn}[\text{Fe}_{0.99}(\text{CN})_6]_{0.95} \cdot 1.92\text{ H}_2\text{O}$  material. By utilizing a high-temperature drying process, they effectively decreased the lattice interstitial water content, leading to a significant enhancement in material performance. At the same time, Peng and his team<sup>[82]</sup> introduced a novel “water-in-salt” nanoreactor approach, which allows for highly controlled crystallization in sealed microreaction environments, enabling the creation of Mn-based PBAs (MnHCF-S-170) with outstanding electrochemical performance without the need for additives. While ball milling is a simple synthesis technique that can effectively reduce crystalline water content and particle size, it encounters two main challenges in practical applications: first, NPs tend to clump together during synthesis, resulting in poorly defined cubic morphologies; second, mass transfer limitations in solid-state reaction systems hinder adequate contact between reactants, preventing complete reactions. These limitations significantly restrict the method’s effectiveness in producing high-performance electrode materials. Therefore, future research should concentrate on resolving two critical issues: controlling particle dispersion and optimizing solid-state reaction kinetics.

#### 4.5. Electrodeposition

Vernon<sup>[83]</sup> developed a novel method for preparing PBAs through electrodeposition, using an acidic electrolyte that includes  $\text{FeCl}_3$ ,  $\text{K}_3[\text{Fe}(\text{CN})_6]$ ,  $\text{H}_3\text{BO}_3$ , and  $\text{KCl}$ . By maintaining a constant potential of 0.3 V (versus SCE) through chronoamperometry, nanowire structures of  $\text{Fe}_4[\text{Fe}(\text{CN})_6]_3 \cdot x\text{H}_2\text{O}$  were effectively deposited on polycarbonate membranes. The mechanism of this process starts with the preferential deposition of sparse PB nuclei on the membrane surface, which then gradually grows into continuous films along the walls of anodic aluminum oxide (AAO) pores through several deposition cycles, ultimately resulting in nanotubular PBAs after the template is etched away. Although this electrochemical method offers distinct advantages for controlling nanostructures, there have been no follow-up studies investigating its potential applications for SIBs. Moreover, the pros and cons of the aforementioned preparation methods are summarized in Table 1.

### 5. Modification Strategies

#### 5.1. Doping

Elemental doping is a valuable approach for enhancing electrochemical performance and lowering the costs of PBAs. Its effectiveness is primarily evident in three ways: First, the introduction of dopant elements significantly improves the electron conduction ability of the PBA structure and decreases charge transfer resistance during electrode reactions by modifying metal coordination environments and adjusting crystal electronic structures.<sup>[84,85]</sup> Second, moderate doping can manage structural defects and optimize lattice parameters, which not only broadens ion transport pathways but also increases the number of redox-active sites and speeds up reaction kinetics.<sup>[49,86]</sup> Most

**Table 1.** A comprehensive evaluation of the benefits and limitations associated with various synthesis methods for PBAs.

Preparation method	Advantages	Disadvantages	Ref.
Coprecipitation	<ul style="list-style-type: none"> <li>• Low cost and scalable.</li> <li>• Simple process.</li> <li>• No high-temperature treatment needed.</li> </ul>	<ul style="list-style-type: none"> <li>• High defect concentration.</li> <li>• Poor crystallinity without chelators.</li> <li>• High water content.</li> </ul>	[62,65,66,68]
Single source	<ul style="list-style-type: none"> <li>• Fewer defects.</li> <li>• Higher Na content.</li> <li>• Low crystalline water.</li> </ul>	<ul style="list-style-type: none"> <li>• Limited to Fe-based PBAs.</li> <li>• NaCN byproduct (toxic).</li> <li>• Limited durability.</li> </ul>	[69–71]
Solvothermal	<ul style="list-style-type: none"> <li>• Precise control over morphology and structure.</li> <li>• Produces uniform particles.</li> <li>• Reduced agglomeration.</li> </ul>	<ul style="list-style-type: none"> <li>• Requires high-pressure reactors.</li> <li>• Low production yield.</li> <li>• Higher equipment cost.</li> </ul>	[75–77]
Ball milling	<ul style="list-style-type: none"> <li>• Solvent-free and energy-efficient.</li> <li>• Low processing temperature.</li> <li>• Suitable for scale-up.</li> </ul>	<ul style="list-style-type: none"> <li>• Poor crystal morphology.</li> <li>• Particle agglomeration.</li> <li>• Incomplete reactions.</li> </ul>	[78,81,82]
Electrodeposition	<ul style="list-style-type: none"> <li>• Direct fabrication on substrates.</li> <li>• Nanostructure controllability.</li> <li>• Template-guided growth.</li> </ul>	<ul style="list-style-type: none"> <li>• Limited reports for SIBs.</li> <li>• Difficult scale-up.</li> <li>• Time-consuming.</li> </ul>	[83]

importantly, doping with certain elements can effectively reduce lattice strain during charge and discharge cycles, minimizing structural degradation under high-current conditions and greatly enhancing the cycling stability of the electrodes.<sup>[42]</sup> Current doping modifications of PBAs can be mainly classified based on the varying properties and mechanisms of the dopant elements.

### 5.1.1. TM Element Displacement

Thanks to the tunable framework structure of PBAs, it is possible to make various substitutions with TMs. In terms of performance, the leading modification strategies currently focus on two main methods: (1) utilizing high-capacity, cost-effective Fe-PBAs and Mn-PBAs as host materials while adding Cu/Ni dopants to improve structural stability; (2) using highly stable Ni-PBAs/Cu-PBAs as matrices and incorporating Mn/V dopants to increase capacity. This “complementary advantages” doping approach offers a promising way to enhance the overall electrochemical performance of PBAs.

In Mn-PBAs, the Jahn-Teller effect associated with Mn<sup>2+</sup> causes distortion in the lattice, which results in the dissolution of Mn and the creation of vacancies in the [Fe(CN)<sub>6</sub>] structure (VFeCN). During phase transitions, an excessive buildup of VFeCN can compromise the integrity of the PBA framework when Na<sup>+</sup> ions are inserted, leading to reduced cycling stability and capacity. By partially replacing Mn<sup>2+</sup> with metal ions that do not exhibit the Jahn-Teller effect, it is possible to effectively reduce Mn dissolution and stabilize the crystal structure, thus improving the cycling stability of Mn-PBAs.<sup>[66,87]</sup>

For instance, Mauro et al.<sup>[88]</sup> successfully combined the beneficial properties of two TMs by adding Co to Mn-based PBAs, achieving a notable discharge capacity of 100 mAh g<sup>-1</sup> at a rate of 0.5 C and an average discharge voltage of 1 V. The Liang<sup>[89]</sup> research group introduced an innovative cation-capture method, using sodium ferrocyanide (Na<sub>4</sub>[Fe(CN)<sub>6</sub>]) as an additional salt in a high-concentration NaClO<sub>4</sub> electrolyte system (Figure 8a,b). This technique effectively repaired Mn vacancy defects in Fe-doped

PBAs (NaFeMnF) that occurred during electrochemical cycling, helping to preserve the structural integrity of the cathode material. As a result, SIBs reached impressive initial discharge capacities of 157 mAh g<sup>-1</sup> at 0.5 A g<sup>-1</sup> and 125 mAh g<sup>-1</sup> at 10 A g<sup>-1</sup>. Gao<sup>[90]</sup> team developed a series of affordable Cu-doped Mn-based PBAs using a sodium citrate-assisted coprecipitation method. The optimized CuHCF-3 material exhibited outstanding electrochemical properties, and its straightforward preparation process indicates significant potential for large-scale production. To test its practical use, 8650 cylindrical cells were created with CuHCF-3 as the cathode and hard C as the anode (Figure 8c). As shown in Figure 8d, this battery system demonstrated a specific capacity of 115.8 mAh g<sup>-1</sup> and an energy density of 391.4 Wh kg<sup>-1</sup> at room temperature, while maintaining stable performance across a wide temperature range (−20 to 55 °C). Additionally, Kong et al.<sup>[91]</sup> successfully created V-doped Mn-PBAs (V<sub>0.5</sub>Mn<sub>0.5</sub>PBA), which utilize the synergistic effects of two high-capacity elements to achieve a high specific capacity of 136.9 mAh g<sup>-1</sup> at 20 mA g<sup>-1</sup> and excellent cycling stability. As presented in Figure 8e,f, the dQ/dV curves of V<sub>0.5</sub>Mn<sub>0.5</sub>PBA over the initial 50 cycles exhibited reduced Mn dissolution. In situ Raman spectroscopy analysis further revealed minimal peak shifts in the Fe—C≡N vibrational modes, collectively demonstrating the structural stabilization effect of V doping (Figure 8g–j).

### 5.1.2. High-Entropy Strategy

In recent years, research on PBAs has shifted from single or dual-metal doping to high-entropy material systems. By applying the design principles of high-entropy alloys, high-entropy PBAs (HE-PBAs) utilize five or more TM elements, each comprising 5–35% of the total composition, to create multicomponent systems with elevated configurational entropy. This high-entropy approach improves material performance through two main mechanisms: (1) Entropy-driven stabilization: The random arrangement of different atoms boosts configurational entropy and lowers Gibbs free energy, which thermodynamically stabilizes the crystal

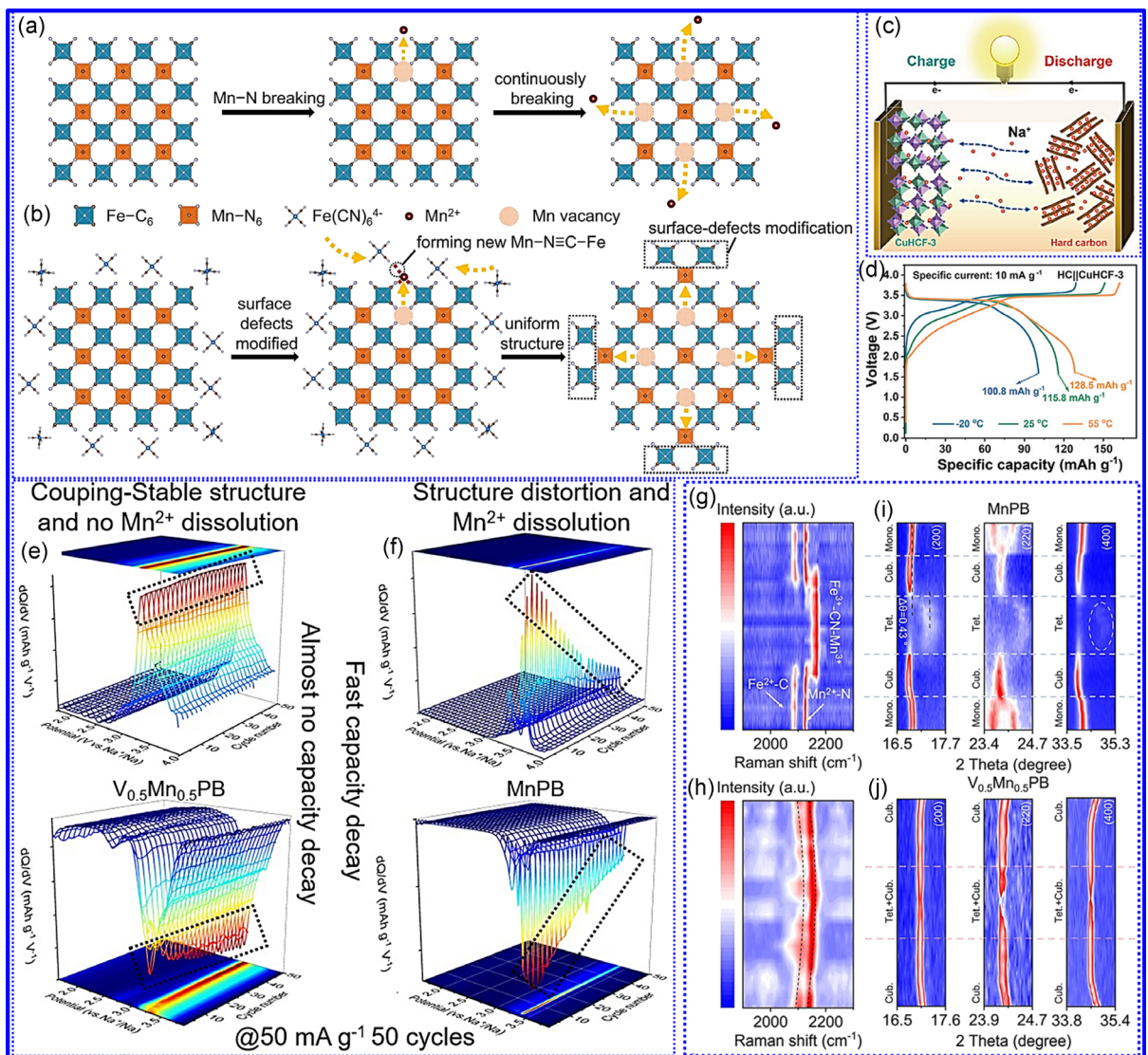


**Figure 8.** a,b) Schematic illustration of the Mn dissolution and the cation trapping processes. Adapted with permission.<sup>[89]</sup> Copyright 2023, Springer Nature. c) Schematic illustration of the HC/CuHCF-3 configuration. d) The potential matchup between CuHCF-3 and HC at 10 mA g<sup>-1</sup>. The wide-temperature (-20 to 55 °C) electrochemical performance of HC/CuHCF-3 full cell. Adapted with permission.<sup>[90]</sup> Copyright 2025, Wiley-VCH. e,f) dQ/dV profiles of charge and discharge processes at the first 50 cycles of V<sub>0.5</sub>Mn<sub>0.5</sub>-PBA and Mn-PBA. g-j) In situ Raman spectra and Intensity contour maps of Mn-PBA and V<sub>0.5</sub>Mn<sub>0.5</sub>-PBA. Adapted with permission.<sup>[91]</sup> Copyright 2025, Wiley-VCH.

structure; (2) Cation “cocktail” effect: The combined effects of various metal ions enhance the electronic structure and coordination environments. When compared to traditional doping methods, high-entropy PBAs exhibit greater phase stability and electrochemical reversibility.

Zhao et al.<sup>[92]</sup> applied the design principle of coordinated ion volume matching by incorporating five TM elements (Ni, Cu, Mn, Co, and Zn) in equal amounts at the M<sub>1</sub> sites of Ni-PBAs, successfully creating HE-PBAs. The resulting full cells demonstrated superior cycling and rate performance compared to traditional single-metal hexacyanoferrate, achieving a capacity of 75 mAh g<sup>-1</sup> at 0.5 C and an 87% retention rate after 1000 cycles at 1C. This research confirms the potential of HE-PBA materials for SIB applications. Inspired by the Rubik’s cube, Peng et al.<sup>[93]</sup>

developed a new type of HE-PBAs (HE-HCF). Characterization showed that this disordered framework, inspired by the Rubik’s cube, significantly improves the Na storage capacity of HE-HCF while providing outstanding cycling stability, exceeding 50,000 cycles. Qian et al.<sup>[94]</sup> further expanded the elemental diversity to synthesize six-element HE-PBAs (H-PBAs) with a “quasi-zero-strain” structural feature, achieving a high-capacity retention of 92.6% after 500 cycles. Comprehensive characterization was conducted to clarify the specific roles of each element in stabilizing the framework and enhancing electrochemical performance. Dai et al.<sup>[95]</sup> creatively combined the high-entropy approach with K-ion doping to produce K<sub>x</sub>(MnFeCoNiCu)[Fe(CN)<sub>6</sub>] (referred to as HE-K-PBA). Thermal expansion simulation analysis in Figure 9a-d indicated that this

material experiences minimal stress variation during discharge, demonstrating that the high-entropy effect effectively balances internal stress distribution. Ultimately, after 1700 cycles at  $1 \text{ A g}^{-1}$ , the capacity retention rate was 90.4%.

However, during the creation of HE-PBAs, differences in binding affinities between TM ions ( $\text{TM}^{2+}$ ) and chelating agents can lead to asynchronous release of metal ions, resulting in phase separation problems. To tackle this significant issue, researchers have come up with creative solutions. He's team<sup>[96]</sup> utilized sodium citrate ( $\text{Na}_3\text{Cit}$ ) as a chelator, successfully producing structurally stable HE-PW that shows a marked reduction in gas evolution during the de/intercalation of Na ions. Meanwhile, the Wang<sup>[67]</sup> research group introduced ascorbic acid as a pH modulator to finely tune the chelation ability of  $\text{Na}_2\text{EDTA}$ , leading to the synthesis of highly crystalline HE-PBAs (Figure 9e-g). These findings offer essential methodological insights for the controlled production of high-entropy materials.

As an important development direction in doped material systems, HE-PBAs have preliminarily demonstrated their ability to simultaneously enhance both specific capacity and structural stability through multicomponent synergistic effects. However, two major scientific challenges persist in this area: First, the electronic interaction mechanisms among various TM elements are not yet fully understood; second, there is a lack of systematic research on the relationship between element selection criteria and optimal doping ratios, which limits the effective design of high-performance HE-PBAs.

### 5.1.3. Active Site Doping

In the research on SIBs cathodes, the amount of  $\text{Na}^+$  in PBAs shows a strong relationship with their electrochemical performance. Long et al.<sup>[97]</sup> established that increasing the  $\text{Na}^+$  content

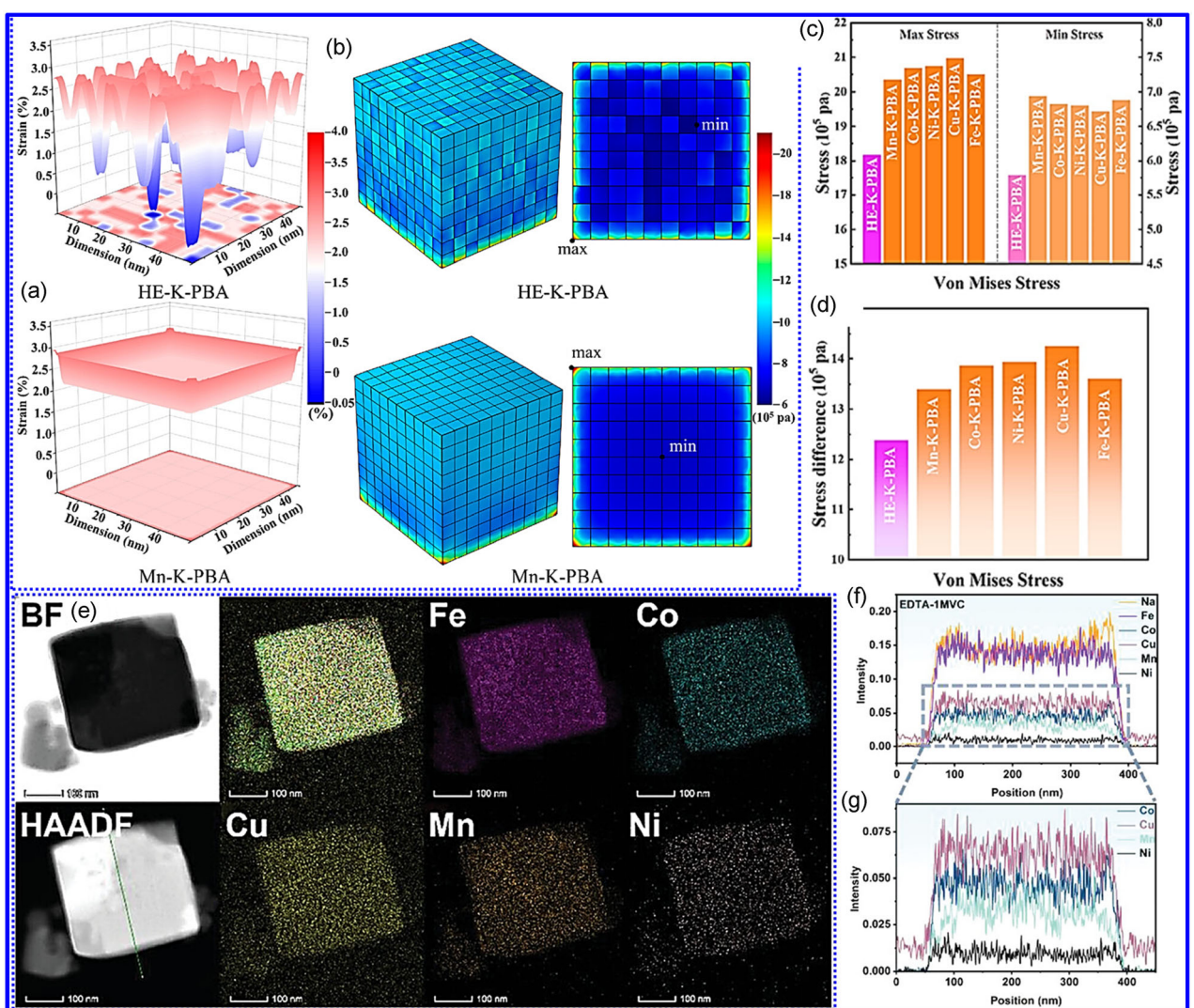


**Figure 9.** a) Distributions of strain of HE-K-PBA and Mn-K-PBA. b) 3D von Mises stress distributions and corresponding ground stress distributions of HE-K-PBA and Mn-K-PBA. c) The maximum and minimum von Mises stress and d) the difference between maximum and minimum von Mises stress of HE-K-PBA, Mn-K-PBA, Co-K-PBA, Ni-K-PBA, Cu-K-PBA, and Fe-K-PBA. Adapted with permission.<sup>[95]</sup> Copyright 2023, American Chemical Society. e) TEM and EDS phase analysis and element mapping of EDTA-1MVC. f,g) EDS line scan spectra of EDTA-1MVC. Adapted with permission.<sup>[67]</sup> Copyright 2024, Wiley-VCH.

effectively stabilizes the crystal structure and improves reversible capacity. These results were later confirmed by Lee<sup>[98]</sup> and Wang,<sup>[99]</sup> who found that PBAs with high Na<sup>+</sup> content and high crystallinity consistently exhibited better electrochemical properties. Building on these findings, researchers have introduced a novel metal-ion doping strategy that differs from traditional doping methods involving TMs. This new approach enhances the structural stability and electrochemical performance of PBAs by replacing Na<sup>+</sup> ions within their framework.

Typically, the structural stability, operating voltage, and capacity of PBA electrode materials are largely influenced by the inherent characteristics of the ions that are inserted. The process of extracting or inserting Na<sup>+</sup> can often lead to irreversible structural damage. To mitigate this problem, Sun et al.<sup>[100]</sup> introduced Ba<sup>2+</sup>, which has a larger ionic radius, into the PBA structure. The larger Ba<sup>2+</sup> can replace Na<sup>+</sup> and function as a "pillar" within the PBA framework. Additionally, Ba<sup>2+</sup> acts as a new "defender" that blocks water molecules from entering the framework, thus improving the stability of PBAs (Figure 10a). By carefully adjusting the concentration of Ba<sup>2+</sup> in the electrolyte, the resulting cathode showed a capacity retention of 96.6% after 150 cycles, while achieving a reversible capacity of 83.41 mAh g<sup>-1</sup> even at a rate of 6 C. Furthermore, Yang et al.<sup>[101]</sup> found that doping with K<sup>+</sup> could expand the PBA lattice and decrease water content, which in turn creates more Na storage sites and broader ion transport pathways. Consequently, the K-doped NiHCF electrode achieved an impressive initial discharge capacity of 87.1 mAh g<sup>-1</sup> at a current of 10 mA g<sup>-1</sup>.

As shown in Figure 10b, Dai et al.<sup>[95]</sup> performed a detailed analysis of the role of K<sup>+</sup> using ex situ time-of-flight secondary ion mass spectrometry (TOF-SIMS), allowing for direct observation of K<sup>+</sup> de/intercalation reactions. To further explore the pillar effect of metal cations in PBAs frameworks, Xu's team<sup>[102]</sup> utilized seawater as a reaction solvent to synthesize PBAs with K<sup>+</sup> and Mg<sup>2+</sup> dopants. Figure 10c illustrates that the Mg<sup>2+</sup> and K<sup>+</sup> ions incorporated into the PBA lattice remain stationary, forming stable K-N and Mg-N bonds that provide structural support, helping to prevent phase transitions and elemental dissolution. The resulting seawater-derived PBA material exhibits remarkable cycling longevity, retaining 80.1% of its capacity after 2400 cycles, and excellent rate capability, with 90.4% capacity retention at 20 C compared to 0.1 C. However, these cation doping methods have primarily focused on lattice expansion and structural support, mainly improving cycling stability and rate capability. The Wang<sup>[103]</sup> research group overcame these traditional limitations by innovatively creating CNT-composited silver hexacyanoferrate nanomaterials (AgHCF@CNTs). During the charge/discharge cycles, the Ag<sup>+</sup>/Ag redox couple acts as an additional redox center, enhancing the capacity of AgHCF@CNTs. Additionally, the Ag NPs formed during discharge attach to the cathode, further improving the material's conductivity (Figure 10d). The well-engineered AgHCF@CNTs cathode ultimately achieves a reversible capacity of 168.4 mAh g<sup>-1</sup> at 50 mA g<sup>-1</sup> and retains 74% of its capacity after 500 cycles at 500 mA g<sup>-1</sup>.

Currently, as a developing modification approach for PBAs, metal cation doping encounters several significant unresolved

challenges related to its mechanisms and practical use. First, the stabilization processes of various metal cations within the PBA structure and their impact on electron conduction and ion diffusion are not well understood. Second, there are no established systematic criteria for selecting appropriate doping ions, such as those based on ionic radius and valence state effects. Future studies need to tackle these essential issues to progress in this area.

## 5.2. Surface Engineering

While cycling, the PBA lattice experiences contraction and expansion due to the extraction and insertion of Na<sup>+</sup>, which causes internal microcracks and structural distortion. This process initiates several negative consequences, such as increased side reactions, reduced electron transfer efficiency, dissolution of TMs, and structural degradation, all of which lead to a decline in cycling performance and capacity. To tackle these issues, surface engineering techniques have shown significant benefits in modifying PBAs.

### 5.2.1. Surface Coating

Surface coating is a straightforward yet effective technique in surface engineering. It is essential to apply a strong and thorough coating layer on PBA particles to tackle issues related to cycling instability and inadequate rate performance.<sup>[104]</sup> However, traditional high-temperature coating techniques (over 350 °C) that involve calcination with conductive materials are not appropriate for PBAs, as they can lead to structural breakdown at high temperatures. This creates a need for new coating strategies for PBAs.<sup>[105]</sup> The optimal coatings should be able to be applied at lower temperatures while ensuring stability.

Certain organic polymers have shown remarkable effectiveness in this area. For instance, Peng et al.<sup>[106]</sup> successfully created hydrophobic PB (PB@TA@ODA) by applying hydrophobic octadecylamine (ODA) chains to PBAs (Figure 11a). Even after being exposed to humid conditions for 7 days, PB@TA@ODA-7D maintained a reversible capacity of 145 mAh g<sup>-1</sup> at a rate of 1C. Kim et al.<sup>[107]</sup> improved the Na<sup>+</sup> storage capacity and rate performance of PB by adding a PEDOT: PSS overlayer, resulting in a reversible capacity of about 112.6 mAh g<sup>-1</sup> at a high-rate of 1220 mA g<sup>-1</sup>. Xue et al.<sup>[108]</sup> enhanced both electronic conductivity and capacity through the in situ polymerization of polypyrrole (PPy) on PBA surfaces. Yi et al.<sup>[109]</sup> significantly increased the Na<sup>+</sup> storage capacity and conductivity of PBAs by applying a polydopamine (PDA) coating. Notably, Fu et al.<sup>[110]</sup> used aminated pyromellitic dianhydride as a coating material, which not only improved conductivity but also effectively reduced the dissolution of TMs in PBAs, achieving impressive results with 73.4% capacity retention after 1000 cycles (Figure 11b-d).

In addition to organic materials, a range of inorganic substances has been effectively used for coating PBA surfaces. For instance, MoS<sub>2</sub> acts as a 2D support that promotes uniform nucleation of PBAs, greatly enhancing the surface area of the material.

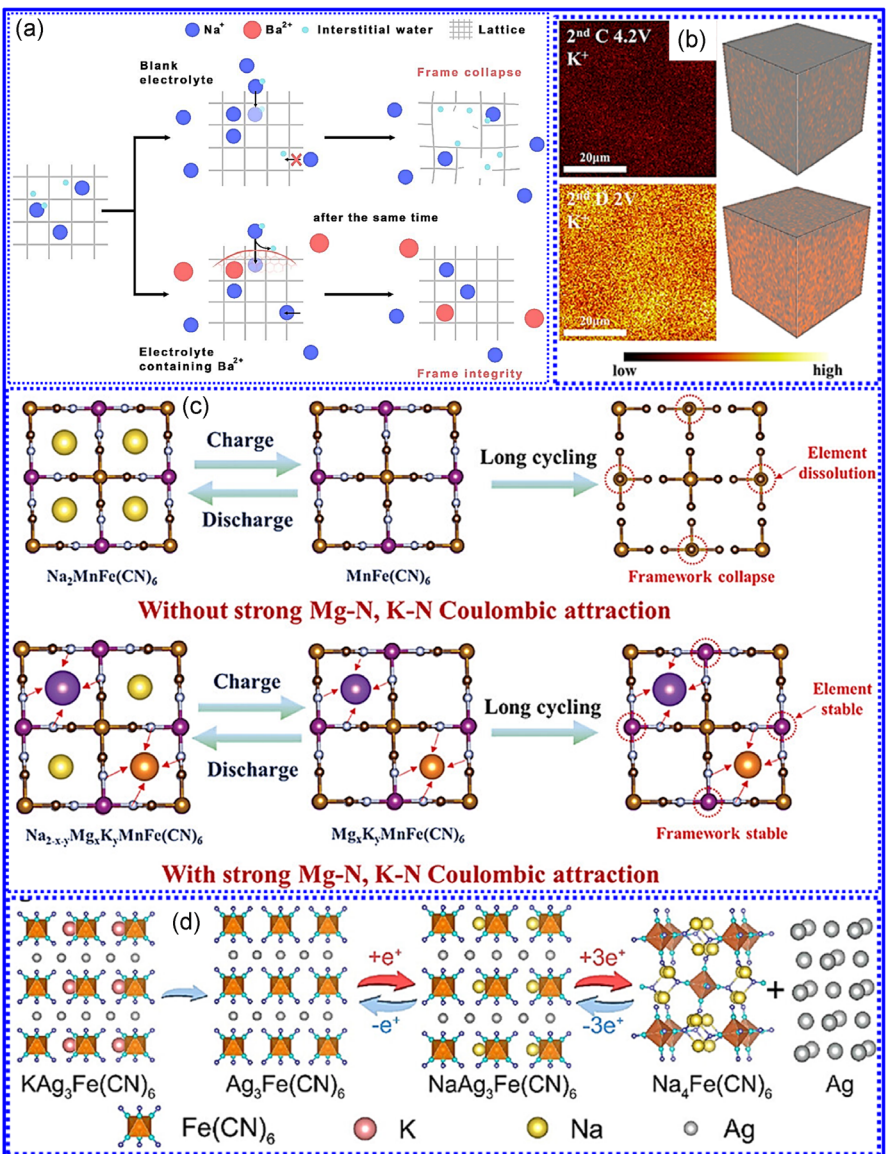


**Figure 10.** a) Schematic diagram of  $\text{Ba}^{2+}$  acting as a "defender" to prevent water molecules from entering the lattice to maintain the framework stability. Adapted with permission.<sup>[100]</sup> Copyright 2023, Elsevier B.V. b) Ex situ TOF-SIMS analysis of HE-K-PBA cathode during the second cycle. Adapted with permission.<sup>[95]</sup> Copyright 2023, American Chemical Society. c) Stabilizing mechanism of the PB framework by  $\text{Mg}^{2+}/\text{K}^+$  co-doping. Adapted with permission.<sup>[102]</sup> Copyright 2024, Wiley-VCH. d) Schematic illustration of the conversion reaction mechanism of the  $\text{AgHCF@CNTs}$  electrode. Adapted with permission.<sup>[103]</sup> Copyright 2024, American Chemical Society.

When utilized as a cathode in SIBs, it can achieve a discharge capacity of up to 177 mAh g<sup>-1</sup>.<sup>[111]</sup>  $\text{ZnO}$  creates a stable core–shell structure with PBAs, showing a discharge capacity of 86.2 mAh g<sup>-1</sup> at 10 A g<sup>-1</sup> and a high reversible capacity of 89.9 mAh g<sup>-1</sup> at 0.2 A g<sup>-1</sup> after 500 cycles.<sup>[112]</sup> The  $\text{Na}_3(\text{VOPO}_4)_2\text{F}$  coating effectively shields PBAs from electrolyte corrosion, maintaining the stability of the framework during cycling.<sup>[113]</sup> Additionally,  $\text{Co}_x\text{B}$  forms a protective skin-like layer on Mn-PBAs, which helps to reduce the dissolution of Mn and prevent the formation of internal cracks during cycling, allowing for 2500 stable charge-discharge cycles.<sup>[114]</sup>

The selection of surface coatings for PBAs offers unique benefits when comparing organic and inorganic materials. Organic

coatings, such as PPy and PDA, are known for their excellent conductivity and strong interfacial adhesion, which significantly improve charge transfer efficiency and help manage lattice strain. However, their vulnerability to degradation from extended structural stress or high temperatures can hinder long-term cycling performance. On the other hand, inorganic coatings like  $\text{MnO}_2$  and  $\text{MoS}_2$ , while often requiring more intricate manufacturing methods, provide greater mechanical strength and chemical stability. These characteristics allow them to effectively prevent the dissolution of TMs and protect against electrolyte corrosion, leading to improved cycling stability. Recent research has been leaning toward organic-inorganic hybrid coating systems, such as the PDA-C bilayer structure developed by Kitchamsetti et al.<sup>[115]</sup>

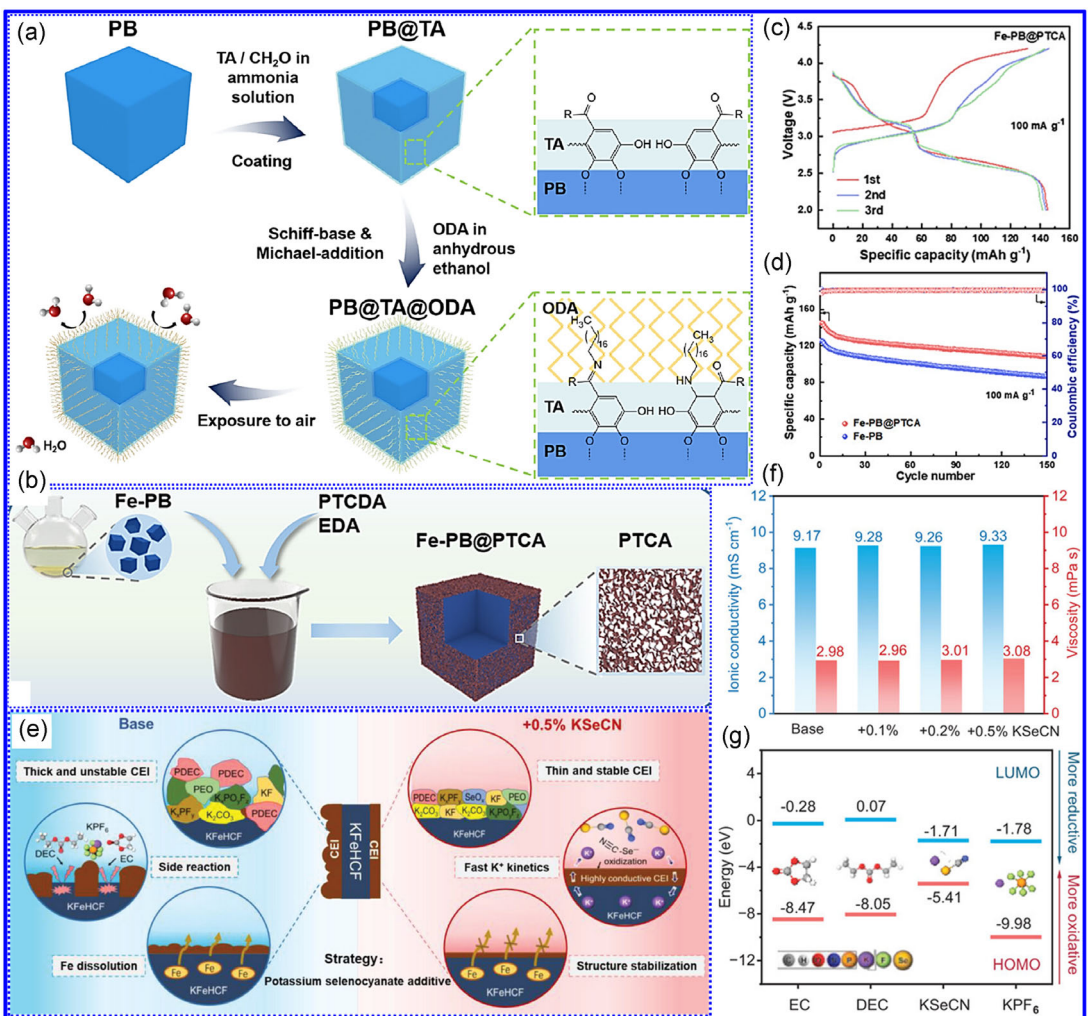


**Figure 11.** a) Schematic illustration of the preparation of hydrophobic PB. Adapted with permission.<sup>[106]</sup> Copyright 2024, American Chemical Society. b) Preparation process and structure schematic illustration of aminated PTCA-coated Fe-PB (Fe-PB@PTCA). c) Charge/discharge profiles of Fe-PB@PTCA at 100 mA g<sup>-1</sup>. d) Cycling performance of Fe-PB@PTCA and Fe-PB at 100 mA g<sup>-1</sup>. Adapted with permission.<sup>[110]</sup> Copyright 2024, Wiley-VCH. e) The schematic diagram showing the effects of KSeCN additive on electrode electrolyte interfacial properties. f) Viscosity and ionic conductivities of the base electrolytes (0.8 m KPF<sub>6</sub>, EC/DEC, v/v = 1:1) with different amounts of KSeCN addition. g) Calculated LUMO and HOMO of conventional solvents and KSeCN. Adapted with permission.<sup>[123]</sup> Copyright 2024, Wiley-VCH.

This design effectively merges the conductive C layer with the adhesive PDA interphase, enhancing both conductivity and stability. This approach offers a fresh perspective on achieving a balance among three essential aspects: charge transport efficiency, structural integrity, and ease of synthesis.

### 5.2.2. Cathode Electrolyte Interphase Construction

The structural and chemical characteristics of the electrode-electrolyte interface play a crucial role in determining the efficiency and stability of electrochemical reactions during charge and discharge cycles.<sup>[116,117]</sup> The thickness and stability of the cathode electrolyte interphase (CEI) that forms on the cathode surface are vital for regulating ion transport. If the CEI is too thick or unstable, it can significantly increase interfacial impedance, hindering both ionic and electronic transfer rates. Additionally,

variations in ion transport rates can occur due to interfacial heterogeneity, which arises from small gaps or uneven distribution of the chemical environment at the interface.<sup>[118–120]</sup> Moreover, unwanted reactions between the electrode surfaces and electrolytes can produce electrochemically inactive byproducts that further obstruct efficient charge transfer. Therefore, optimizing the composition of the CEI can effectively reduce side reactions and enhance interfacial uniformity, leading to improved performance of cathode materials.

Incorporating functional additives into the electrolyte is an effective and practical modification approach. Typically, these additives are preferentially oxidized during the charging process, leading to the creation of a customized CEI on the surfaces of PBAs. Various additives result in the development of different CEIs, each serving unique purposes. For instance, adding 1 wt% of AlCl<sub>3</sub> as a Lewis acid creates a fluffy Al<sub>2</sub>O<sub>3</sub> layer on PBAs, which selectively prevents water molecules from

penetrating while allowing  $\text{Na}^+$  transport channels to remain open, achieving a capacity of  $111 \text{ mAh g}^{-1}$  even at a rate of  $1\text{C}$ .<sup>[121]</sup> When the additive concentration is increased to 5 wt%, a poly(ethylene carbonate) interface layer forms, which effectively reduces interfacial side reactions and the growth of Na dendrites, resulting in a cycle life exceeding 4000 cycles.<sup>[122]</sup> Additionally, the potassium selenocyanate (KSeCN) additive, with its elevated HOMO (highest occupied molecular orbital) energy level, generates a Se-rich layer on PBAs that significantly inhibits surface decomposition and improves conductivity (Figure 11e–11g).<sup>[123]</sup>

Additives that generate inorganic materials, such as cresyl diphenyl phosphate (CDP) and adiponitrile (ADN), produce inorganic-rich CEI layers that greatly reduce structural damage during PBA cycling (Figure 12a). Even after 1400 cycles, these batteries maintained a capacity retention rate of 85.62%.<sup>[124]</sup> Importantly, the CEI films created by CDP-type additives can also activate low-spin Fe ion sites within the PBA structure while forming flame-retardant barriers. As a result, batteries with the appropriate amount of CDP showed a capacity of  $106.1 \text{ mAh g}^{-1}$  at  $1\text{C}$  and retained 83.1% of their capacity after 700 cycles.<sup>[125]</sup> Sodium difluoro(oxalato)borate (NaDFOB) establishes a boron/fluorine-enhanced passivation interface that prevents dendrite formation

and electrolyte decomposition (Figure 12b).<sup>[126]</sup> In addition to electrolyte modifications, Ye's team<sup>[104]</sup> introduced a pre-sodiation method that creates a  $\text{NaF}$ -rich interfacial layer, offering PBAs a protective barrier against organic solvent damage, resulting in an impressive cycling life of 3000 cycles.

### 5.3. Composite Strategy

The strategy of using composite materials offers a valuable method for enhancing the performance of PBAs. By creating core–shell structures or hybrid networks with various functional materials, PBA composites can combine the benefits of different elements. This allows the composites to demonstrate excellent conductivity, fast ion migration, outstanding rate capability, and greatly improved cycle life, providing a crucial solution for the advancement of high-performance SIB cathode materials.

#### 5.3.1. Carbon Composite

The integration of C materials with PBAs is a notable modification strategy, where C functions as both a conductive matrix to improve electron transport and a 3D network to prevent the

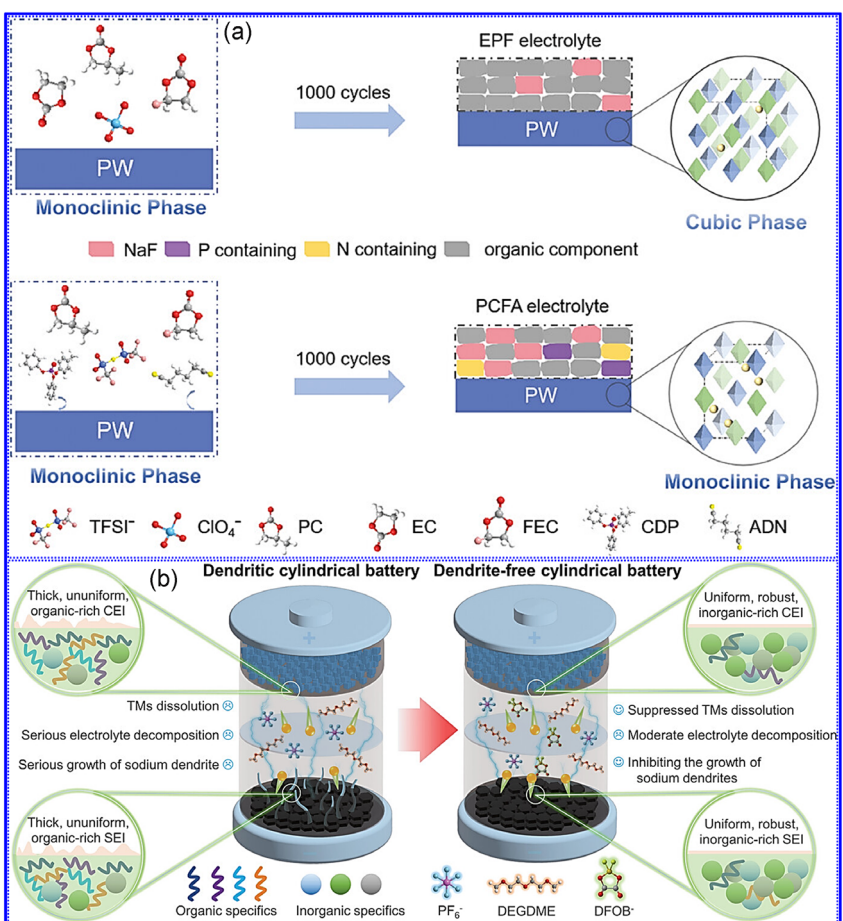


**Figure 12.** a) Schematic illustration of electrolyte and PW structure evolution in PCFA and EPF. Adapted with permission.<sup>[124]</sup> Copyright 2024, Wiley-VCH.  
b) Schematic diagram of dendrite free SIBs designed through electrolyte interface engineering. Adapted with permission.<sup>[126]</sup> Copyright 2024, Wiley-VCH.

agglomeration of active particles.<sup>[127,128]</sup> Throughout electrochemical cycling, C helps maintain the structural stability of the electrode and reduces volume fluctuations in PBAs during ion (de)intercalation by providing elastic buffering, which enhances cycling stability.<sup>[129,130]</sup> This composite method effectively optimizes the pathways for electron and ion conduction while offering mechanical support, resulting in a significant improvement in the performance of PBA electrodes.

Ketjen Black (KB), known for its high specific surface area (SSA) and excellent conductivity, is frequently used as a conductive additive in PBAs electrodes. For instance, Jiang et al.<sup>[131]</sup> successfully integrated well-formed PBAs cubes with a C matrix using an acid-assisted technique, which greatly improved electrical conductivity and  $\text{Na}^+$  intercalation kinetics. The resulting PB@C composite retained a capacity of 90 mAh g<sup>-1</sup> even at an extremely high rate of 90C and demonstrated remarkable long-term cycling stability over 2000 cycles. Wang's team<sup>[132]</sup> further advanced this by combining a high-entropy approach with C coating to create 3D C-encapsulated HE-PBAs (HE-PBAs@C), which effectively reduced lattice distortion and enhanced conductivity. However, while KB-based composites are effective in improving conductivity and cycling stability, they often fall short in capacity performance. This issue can be mitigated by increasing the volumetric/mass ratio of electrochemically active materials. A promising alternative is to combine PBAs with CNTs, which provide excellent conductivity, chemical stability, and high SSA.<sup>[133]</sup> As illustrated in Figure 13a, Zhang et al.<sup>[134]</sup> successfully created 3D CNT network-bridged hetero-structured Ni-Fe-S NCs (Ni-Fe-S-CNT) composites through a combination of coprecipitation and sulfurization heat treatment. The unique 3D hierarchical structure and conductive network significantly reduced ion diffusion distances and enhanced conductivity, resulting in a charge capacity of 431 mAh g<sup>-1</sup> at 0.1 A g<sup>-1</sup> for SIBs. Meanwhile, Lee's team<sup>[133]</sup> employed a chelator-assisted method to develop PW-CNT composites, which not only showed a significant reduction in crystallographic defects and water content but also provided excellent Na storage capacity, cycling stability, and energy density. At a rate of 10 C, the PW-CNT composite cathode achieved a high reversible capacity of 133 mAh g<sup>-1</sup>.

Furthermore, graphene has proven to be an excellent composite matrix for enhancing the performance of PBAs due to its distinctive 2D structure and numerous surface-active sites. Kang's team<sup>[135]</sup> discovered a reversible solid-solid interfacial storage mechanism in PBAs/reduced graphene oxide (rGO) composites, where the separation of electron and ion storage/transport at the interface allows for both high capacity and rapid kinetics (Figure 13b-g). The Jiang<sup>[136]</sup> research group employed rGO as a template for epitaxial growth, guiding PBAs to form truncated cubic shapes with extremely low defect concentrations (< 0.08 mol<sup>-1</sup>), which significantly improved the  $\text{Na}^+$  diffusion coefficient. Additionally, Wang et al.<sup>[137]</sup> showed that incorporating rGO enhances the electrochemical activity of low-spin Fe sites within the PBA framework, achieving a specific capacity of 148.4 mAh g<sup>-1</sup> at 0.1 A g<sup>-1</sup>. Together, these studies highlight the various roles of graphene in influencing the electronic structure, crystallographic defects, and interfacial kinetics of PBAs.

### 5.3.2. Core-Shell Structure

PBAs frequently show a compromise between capacity and stability: materials with high capacity tend to experience structural deterioration with repeated  $\text{Na}^+$  extraction and insertion, whereas those with lower capacity usually exhibit better cycling stability. To take advantage of the structural similarities in PBAs, an *in situ* composite approach can be utilized to create core–shell structures, where high-capacity PBAs serve as the core and high-stability PBAs form the shell. This configuration maintains the core's high-capacity features while improving overall structural stability through the protective shell, effectively reducing lattice strain during cycling without hindering ion transport efficiency.

Figure 13h clearly depicts the process of forming core–shell PBAs. Initially, metal ions adhere to templates created by the electrostatic interactions between high-concentration polymers and acidic radicals. In a system where  $\text{Mn}^{2+}$  and  $[\text{Fe}(\text{CN})_6]^{4-}$  coexist, the competition between citrate and cyanide ions significantly slows down nucleation rates, which helps in producing low-defect, well-defined cubic PBM cores.<sup>[138]</sup> Following this, excess PVP surrounds the nucleated PBM surfaces, limiting further growth of the particles while also creating internal cavities. With the combined effects of PVP and sodium citrate, a high-quality PBN shell is accurately formed. Ultimately, taking advantage of the open framework structure and cyano-bridging properties, the PBN shell and PBM core establish a stable hierarchical core–shell structure through interfacial cyanometallate bonding.

To tackle the challenges associated with traditional core–shell synthesis, researchers have created several streamlined preparation methods. Gebert's team<sup>[139]</sup> took advantage of the selective coordination properties of chelating agents for  $\text{Mn}^{2+}$  and  $\text{Ni}^{2+}$  to facilitate uniform epitaxial growth of Ni-HCF shells on Mn-HCF surfaces, thereby simplifying the synthesis process by controlling reaction kinetics. Ma's group<sup>[140]</sup> successfully synthesized PBN-coated PBM core–shell structures (PBM@PBN) using an *in situ* ion exchange method, where the PBN shell effectively prevented the dissolution of  $\text{Mn}^{2+}$  and demonstrated over 800 cycles, indicating strong scalability potential due to its straightforward preparation. Additionally, these core–shell designs have been applied to various PBA systems. For example, Kong successfully synthesized PBN-coated PBM core–shell structures (PBM@PBN) using an *in situ* ion exchange method, where the PBN shell effectively prevented the dissolution of  $\text{Mn}^{2+}$  and demonstrated over 800 cycles, indicating strong scalability potential due to its straightforward preparation. Additionally, these core–shell designs have been applied to various PBA systems. For instance, Kong et al.<sup>[141]</sup> developed Co-HCF@Fe-HCF core–shell materials that maintained a specific capacity of 54.8 mAh g<sup>-1</sup> at high 20C rates, while Lee's team<sup>[142]</sup> created V/Fe@Cu/Fe-PBAs that improved both cycling stability and power characteristics through shell modification. Nevertheless, the full advantages of these structural designs have yet to be fully realized due to inadequate lattice alignment between the chemically different core and shell components, along with a limited understanding of the mechanisms behind core–shell formation.

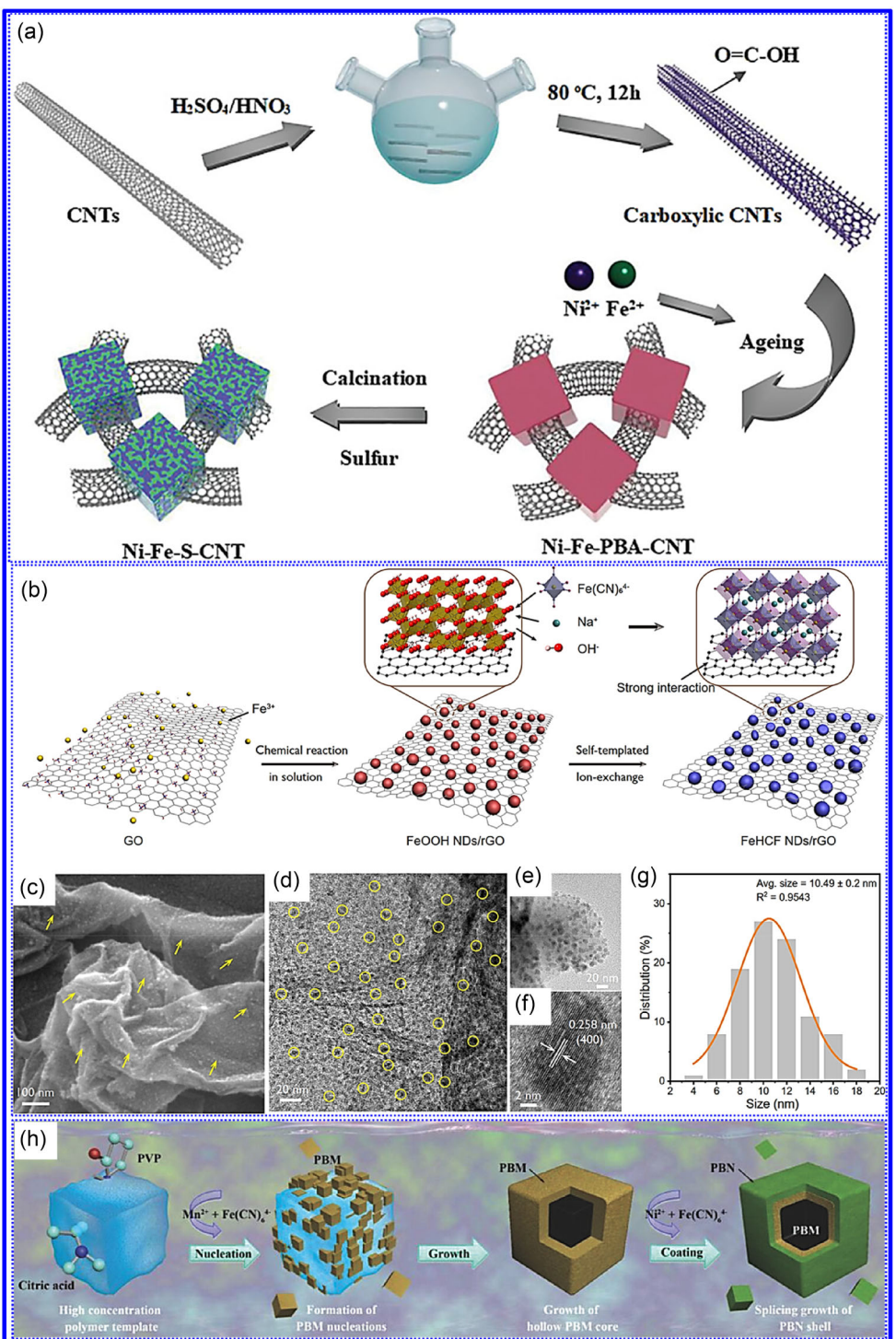


**Figure 13.** a) Schematic of the preparation of 3D hetero-structured bimetallic sulfide ( $\text{Ni}_x\text{Fe}_y\text{S}$ ) encapsulated in N-doped porous C cube interconnected with CNT (denoted as Ni-Fe-S-CNT). Adapted with permission.<sup>[134]</sup> Copyright 2020, Wiley-VCH. b–g) Synthesis process and microstructural analyses of FeHCF NDs/rGO. Adapted with permission.<sup>[135]</sup> Copyright 2022, American Chemical Society. h) Schematic illustration of formation process of regular heterogeneous HCS-PBMN structure. Adapted with permission.<sup>[138]</sup> Copyright 2018, Wiley-VCH.

Addressing these challenges, Zuo<sup>[143]</sup> utilized a one-step approach to create lattice-matched  $\text{MnFe-HCF@MnFe-HCF}$  core-shell structures and provided a theoretical explanation of how the Mn content affects core–shell development. The resulting

$\text{MnFe-HCF@MnFe-HCF}$  demonstrated a high capacity of  $131 \text{ mAh g}^{-1}$  at a current of  $50 \text{ mA g}^{-1}$  and maintained a discharge capacity of approximately  $100 \text{ mAh g}^{-1}$  even at  $1600 \text{ mA g}^{-1}$ . Additionally, Hu<sup>[144]</sup> and colleagues applied the Irving–Williams

series to manage the competitive coordination among  $[\text{Fe}(\text{CN})_6]^{4-}$ ,  $\text{Ni}^{2+}$ ,  $\text{Fe}^{2+}$ , and  $\text{Mn}^{2+}$ , successfully facilitating the *in situ* growth of Ni–Fe mixed PBA shells on the surfaces of Mn-HCF. These investigations offer systematic preparation techniques and mechanistic understanding for the development of high-performance core-shell PBAs.

#### 5.4. Morphology Control

The bulk solid-state structure of PBAs generally results in limited ion transport kinetics, which is mainly observed as a notable reduction in diffusion rates as the depth of  $\text{Na}^+$  insertion increases. To tackle this issue, scientists have devised several synthesis methods focused on enhancing SSA and minimizing cation migration distances to produce PBAs with improved kinetics. These methods for controlling morphology can be divided into three primary categories: managing crystal phase and size, creating hollow or porous structures, and developing nanoflower (NF) architectures.

##### 5.4.1. Crystal Phase and Size Control

In the production of PBAs, conventional coprecipitation techniques often result in irregular shapes and structural flaws due to the rapid rates of ion combination, which can severely affect the materials capacity and stability. The use of chelating agents like citrate and  $\text{Na}_2\text{EDTA}$  can effectively slow down the ion combination process, leading to the formation of well-defined cubic PBAs crystals. Additionally, the size of PBAs particles, which can range from nanometers to several micrometers, has a significant impact on their electrochemical performance. To explore the relationship between size and performance, Nazar<sup>[145]</sup> carefully adjusted the ratio of TM salts to citrate, successfully creating PBAs particles that ranged from 20 to 160 nm and over 1.5  $\mu\text{m}$ . The 20 nm samples, in particular, demonstrated nearly theoretical specific capacity and excellent cycling stability. Furthermore, spherical structures provide benefits over traditional cubic shapes due to their lower surface-to-volume ratios and isotropic properties, which generally result in higher tap densities. Slurries made from spherical particles also show improved fluidity, dispersibility, and processability, enhancing rheological properties and allowing for the creation of high-mass-loading electrodes. This advantage was confirmed by Fan,<sup>[146]</sup> whose recrystallization-driven method produced quasi-spherical monoclinic Co–Fe hexacyanoferrate (CFHCF) with remarkable Na storage capabilities across a wide temperature range (−20 to 50 °C), underscoring its potential for industrial applications. These strategies for controlling morphology are essential for aligning the inherent properties of PBAs with practical manufacturing needs.

##### 5.4.2. Hollow/Porous Structures

The construction of hollow or porous structures in PBAs presents distinct benefits for improving electrode performance.

These designs greatly enhance the active interfacial areas for ion transport due to their natural voids, while also providing materials with remarkable volume-strain resilience. The combined effects of ultrathin shells and high SSAs optimize both ion transport kinetics and surface redox reaction rates. Notably, the carefully engineered cavities and uniform characteristics of these structures effectively accommodate volume changes during charge and discharge cycles. Currently, the production of PBA hollow structures mainly depends on four key methods: hard templating, soft templating, template-free self-assembly, and sacrificial templating. Researchers have successfully created innovative morphologies using these techniques. For instance, Lou et al.<sup>[147]</sup> achieved controlled synthesis of Co-Fe PBA cages in various shapes by carefully managing growth kinetics (Figure 14a–c). Wei et al.<sup>[148]</sup> developed a unique stepwise hollow cubic framework that shortens  $\text{Na}^+$  diffusion paths, boosts electronic conductivity, and enhances redox reactions (Figure 14d). As a result, the PBAs electrode demonstrated ultra-high-rate capacities of 149.2 and 35  $\text{mAh g}^{-1}$  at 0.1 and 100 C, respectively. Meanwhile, Hu et al.<sup>[149]</sup> produced unique single crystalline nano-frameworks that exhibited stable cycling life exceeding 500 cycles (Figure 14e). Additionally, Chou's team<sup>[150]</sup> recently published a comprehensive review on PBA hollow structures, offering essential theoretical insights and technical references for their use in energy storage and conversion applications.

##### 5.4.3. Nanoflower Architectures

The NF structure is a unique method for controlling morphology that converts pure PBA NCs into hierarchical architecture made up of stacked nanosheets (NSs) through a chemical etching process. This method usually involves using acid or base etchants to selectively dissolve defective areas in the crystals while maintaining the integrity of the lattice framework, thereby creating intricate microstructures on or within the material. During the etching process, the cube edges with higher surface energy are preferentially etched, followed by a dissolution-recrystallization process that elongates the etched areas along each surface, leading to the development of NSs structures. The etched PBAs have a higher SSA due to the NF architecture, which allows for greater interaction with electrolytes and improved ion diffusion coefficients.<sup>[151]</sup> Notably, the surfaces of the etched NSs are abundant in active sites, and their anisotropic growth properties provide the material with rapid surface redox kinetics and excellent structural stability. For instance, Mai et al.<sup>[152]</sup> synthesized Ni hexacyanoferrate (NiHCF-etch) with a NF shape through NaOH etching, which increased Na storage sites and exhibited remarkable rate capability of 71  $\text{mAh g}^{-1}$  at 44.4 C, along with cycling stability exceeding 5000 cycles. The formation process of the NF structure is illustrated in Figure 14f–h. Additionally, Zuo et al.<sup>[153]</sup> successfully created 3D NF-shaped  $\text{Na}_2\text{FeFe}(\text{CN})_6$  using a straightforward directed self-assembly technique. This morphology minimized defects and crystalline water content in  $\text{Na}_2\text{FeFe}(\text{CN})_6$ , significantly enhancing its electrochemical performance.

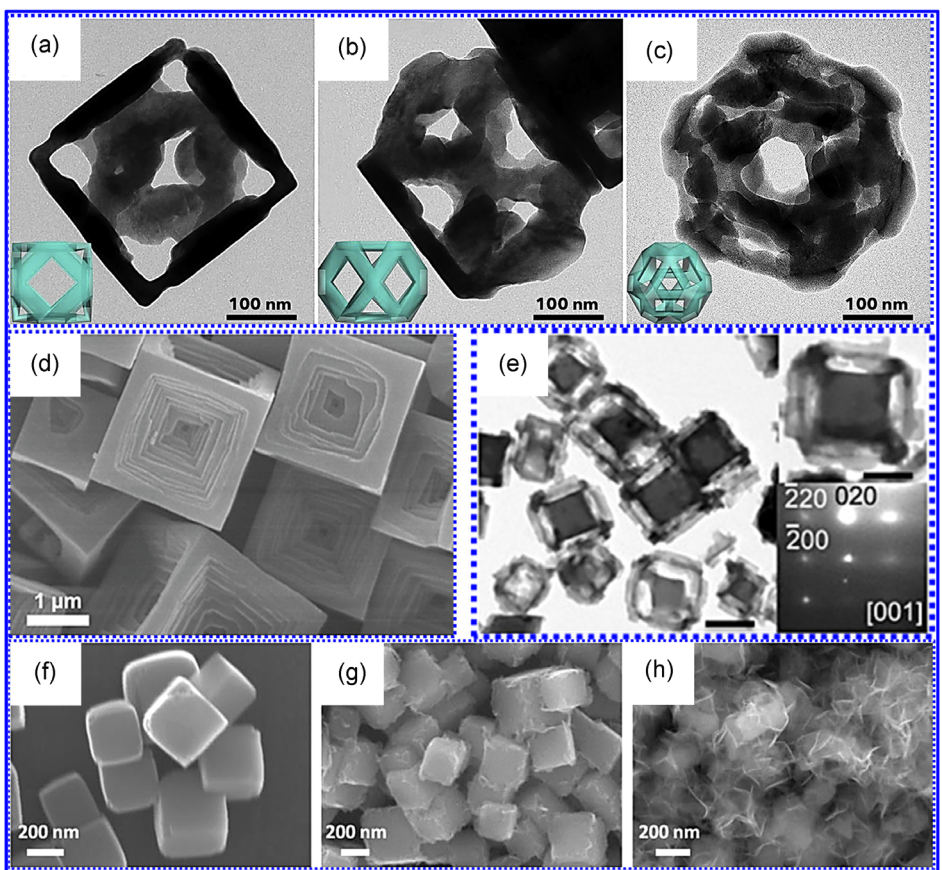


**Figure 14.** a–c) Characterization and TEM images of the CoFe-PBA frames with an average size of 300 nm and a fully open structure. Insets are corresponding schematic models. Adapted with permission.<sup>[147]</sup> Copyright 2018, Cell Press. d) FE-SEM images of stepwise hollow FeHCFe nanoframes. Adapted with permission.<sup>[148]</sup> Copyright 2020, Wiley-VCH. e) TEM images of NiFe(II)-PBA nanoframes. Adapted with permission.<sup>[149]</sup> Copyright 2016, Wiley-VCH. FE-SEM images of the Ni-HCF products after the etching time for f) 0 h, g) 0.5 h, and h) 6 h. Adapted with permission.<sup>[152]</sup> Copyright 2017, American Chemical Society.

Moreover, the pros and cons of the aforementioned modification strategies are summarized in **Table 2**.

## 6. Conclusion and Outlook

This review offers a detailed examination of PBAs as a key cathode material for SIBs, discussing their basic structure, Na ion transport pathways, and real-world applications in energy storage. Additionally, we methodically explore different synthesis techniques for PBAs and evaluate approaches to enhance their inherent properties, with the goal of improving specific performance metrics of PBA-based batteries. **Table 3** presents a comparative analysis of the performance of PBAs modified by different modification strategies, highlighting significant advances in electrochemical performance parameters in SIBs. Due to their distinctive structural features, PBAs hold considerable promises for a wide range of applications, potentially serving as a complement or alternative to LIBs in certain areas. Nevertheless, there are still several challenges that need to be addressed regarding current PBA materials (**Figure 15**). The next section will focus on these challenges and possible solutions, while also examining their advancement towards commercial use.

## 6.1. Improve Preparation Methods

The electrochemical performance of PBAs is primarily influenced by their metal composition, the concentration of lattice vacancies, and the amount of crystalline water, all of which are directly affected by the synthesis methods used. The coprecipitation method is the most widely utilized due to its cost-effectiveness, simplicity, lack of high-temperature requirements, and good scalability. However, achieving well-crystallized PBAs with this method necessitates a significant amount of chelator additives, which can increase costs and introduce impurities during large-scale production. The single source method minimizes the need for chelators while still benefiting from coprecipitation, but it is limited to the synthesis of Fe-PBAs and produces highly toxic NaCN byproducts, which poses a serious challenge for industrial use. Although solvothermal methods allow for precise control over the synthesis of PBAs and yield well-dispersed particles, their high equipment costs and low production yields hinder mass manufacturing. In contrast, ball milling shows great promise for large-scale production due to its short processing time, low reaction temperatures, and ease of operation. Importantly, ball-milled PBAs retain their structural integrity without excessive crystalline water, which greatly improves stability.

**Table 2.** A comprehensive evaluation of the benefits and limitations associated with various modification strategies for PBAs.

Modification strategy	Advantages	Disadvantages	Ref.
Surface engineering	<ul style="list-style-type: none"> <li>Mitigates transition metal (TM) dissolution.</li> <li>Enhances electronic conductivity.</li> <li>Stabilizes electrode–electrolyte interface.</li> <li>Reduces side reactions and dendrite formation.</li> </ul>	<ul style="list-style-type: none"> <li>High-temperature coatings may damage structure.</li> <li>Some organic coatings lack long-term durability.</li> <li>Long-term cathode-electrolyte interphase evolution not fully understood.</li> <li>Additive optimization is challenging.</li> </ul>	[106,124,126]
Composite strategy	<ul style="list-style-type: none"> <li>Enhances electronic/ionic conductivity.</li> <li>Suppresses particle agglomeration.</li> <li>Reduces lattice strain.</li> <li>Protects high-capacity core with stable shell.</li> <li>Improves rate performance.</li> <li>Balances capacity and stability.</li> </ul>	<ul style="list-style-type: none"> <li>Difficult to achieve perfect lattice matching.</li> <li>Interface stress may emerge during cycling.</li> <li>High C content may dilute active mass.</li> </ul>	[134,135,138]
Morphology control	<ul style="list-style-type: none"> <li>Shortens diffusion paths.</li> <li>Increases surface area.</li> <li>Enhances redox kinetics.</li> </ul>	<ul style="list-style-type: none"> <li>Complex synthesis.</li> <li>Possible structural instability at high voltages.</li> </ul>	[147–149]
Doping	<ul style="list-style-type: none"> <li>Enhances electronic conductivity.</li> <li>Reduces lattice strain. Improves structural stability.</li> <li>Increases redox-active sites.</li> </ul>	<ul style="list-style-type: none"> <li>Difficult to optimize doping ratios.</li> <li>Complex elemental interaction mechanisms.</li> <li>May introduce compositional inhomogeneity.</li> </ul>	[89–91]

**Table 3.** A comparative assessment of the electrochemical performance of PBAs modified through diverse modification techniques.

Electrodes	Specific capacity	Cycle stability	Modification strategies	Ref.
K-PBA	128 mAh g <sup>-1</sup> at 25 mA g <sup>-1</sup>	81% after 300 cycles at 1 A g <sup>-1</sup>	Morphology control	[163]
Fe <sup>III</sup> [Fe <sup>III</sup> (CN) <sub>6</sub> ]	121.4 mAh g <sup>-1</sup> at 10 mA g <sup>-1</sup>	–	Morphology control	[164]
Na <sub>1.5</sub> Cu <sub>0.038</sub> Fe <sub>0.691</sub> [Fe(CN) <sub>6</sub> ]	135.7 mAh g <sup>-1</sup> at 1000 mA g <sup>-1</sup>	78.5% after 200 cycles at 500 mA g <sup>-1</sup>	Morphology control	[85]
Mn-PBA with Zn ion substitution	104.7 mAh g <sup>-1</sup> at 5 C	88.1 mAh g <sup>-1</sup> in 300 cycles at 1 C	Doping	[165]
[K <sub>0.444(1)</sub> Na <sub>1.414(1)</sub> ][Mn <sub>3/4</sub> Fe <sub>5/4</sub> ](CN) <sub>6</sub>	110 mAh g <sup>-1</sup> at 0.3 C	99% after 300 cycles at the rate of 1 C	Doping	[166]
Na <sub>x</sub> Ba <sub>y</sub> Fe[Fe(CN) <sub>6</sub> ]	83 mAh g <sup>-1</sup> at 6 C	87.22% after 150 cycles at 6 C	Doping	[100]
PB@TA@ODA	94 mAh g <sup>-1</sup> at 30 C	76.6% after 100 cycles at 1 C	Surface engineering	[106]
PB@GO-PVP(MR)	165.2 mAh g <sup>-1</sup> at 1 C	–	Surface engineering	[167]
Fe/MnHCF	134.2 mAh g <sup>-1</sup> at 10 mA g <sup>-1</sup>	95.5% after 400 cycles at 1 A g <sup>-1</sup>	Composite strategy	[168]
HCS-PBMN	123 mAh g <sup>-1</sup> at 50 mA g <sup>-1</sup>	–	Composite strategy	[169]
Na <sub>x</sub> Ni <sub>y</sub> Mn <sub>1-y</sub> Fe(CN) <sub>6</sub> ·nH <sub>2</sub> O	110 mAh g <sup>-1</sup> at 0.2 C	93% after 1000 cycles at 5 C	Composite strategy	[53]

Nonetheless, two main challenges remain for industrial implementation: the aggregation of NPs during synthesis, which hinders the formation of well-defined crystalline cubes, and mass transfer limitations in solid-state reaction systems that result in incomplete contact between reactants and partial reactions. Overcoming these challenges is crucial for enhancing the application of ball milling in this context.

## 6.2. Vacancies Remediation

PBAs are usually produced through rapid precipitation techniques, which can lead to the introduction of various defects and vacancies in their open crystal structures. A high number of vacancies can negatively impact the material's performance by increasing structural instability during cycling, which may result in framework collapse. Additionally, these vacancies can trap water molecules, hindering Na<sup>+</sup> transport and slowing down reaction kinetics.<sup>[85,154]</sup> Moreover, vacancies in [Fe(CN)<sub>6</sub>]<sup>4-</sup> limit the effective use of low-spin Fe (Fe-1s) redox reactions, ultimately decreasing reversible capacity. Recent research has shown that strategies like controlling synthesis rates and elemental doping can significantly reduce

vacancy defects in PBAs, although completely eliminating them remains difficult.<sup>[155,156]</sup> To tackle this issue, future research should concentrate on three main areas: (1) systematically studying the mechanisms of vacancy formation across various synthesis and modification techniques to provide theoretical insights for better control; (2) thoroughly examining the relationship between vacancy concentration and electrochemical performance indicators (such as ionic conductivity, structural stability, and capacity retention) to establish quantitative links; and (3) investigating the dynamic changes of vacancies during electrochemical cycling to create in situ repair methods that allow for spontaneous vacancy filling through electrolyte design or interface engineering. These studies will offer new perspectives for the precise management of vacancy defects and promote the advancement of high-performance PBA materials.

## 6.3. Reduce Crystalline Water

Traditional synthesis of PBAs is usually performed in water-based solutions, which inevitably incorporates crystalline water into the structure.<sup>[157–160]</sup> This crystalline water can lead to several

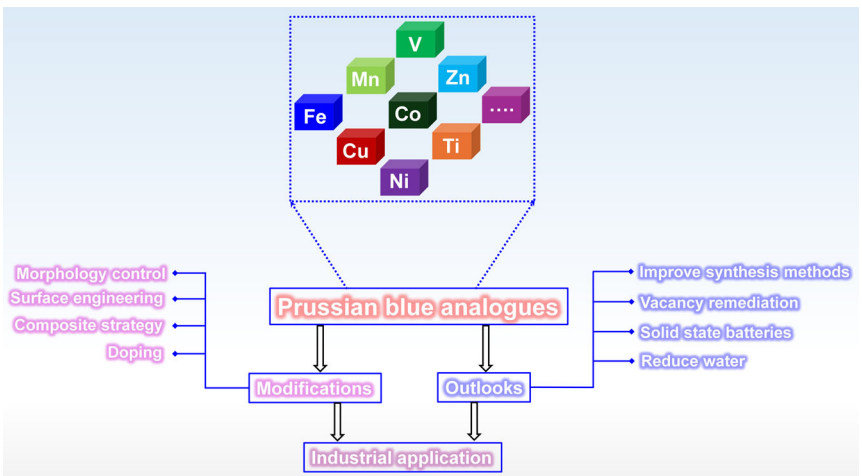


Figure 15. Problems faced by the further application of PBAs.

negative consequences: (1) During the process of ion insertion and extraction, excessive crystalline water can hinder the movement of guest ions, resulting in structural failure and a significant drop in Coulombic efficiency and cycling stability. (2) Remaining water molecules can react with organic electrolytes, impairing electrochemical performance. (3) More importantly, some of these reactions can produce gases, leading to battery swelling and serious safety risks. However, research by Ge et al.<sup>[158]</sup> has shown that small amounts of crystalline water can actually improve the structural stability of PBAs. This indicates that crystalline water might have beneficial effects in PBAs, highlighting the need for further research into how water molecules affect the crystal structure, electrochemical performance, and safety of PBAs for the advancement of high-performance materials. To remove water, ball milling is an effective method, as nonaqueous synthesis can largely avoid water incorporation. Additionally, innovative water-removal techniques have been developed. For instance, Xu et al.<sup>[161]</sup> introduced a “ligand pre-exchange strategy” where EG replaces water in  $[\text{Fe}(\text{H}_2\text{O})_6]^{2+}$ , creating a water-deficient solvation structure  $[\text{Fe}(\text{EG})_x(\text{H}_2\text{O})_{6-x}]^{2+}$  that minimizes both coordinated water and vacancy defects, resulting in high-quality PBA crystals. Ge et al.<sup>[158]</sup> also successfully removed water by applying controlled thermal treatment to PBAs at specific temperatures.

#### 6.4. Solid-State Batteries

Combining PBAs with Na metal anodes can greatly improve energy density, but this setup encounters practical issues such as dendritic Na growth and safety concerns associated with liquid electrolytes.<sup>[82]</sup> A promising approach to create high-energy-density and safe SIBs is to substitute flammable liquid electrolytes with solid-state alternatives while using Na metal anodes. Solid electrolytes offer enhanced safety and excellent mechanical properties, allowing for stable battery performance in extreme conditions, such as high or low temperatures, mechanical stress, or high-pressure situations.<sup>[162]</sup> Nevertheless, significant challenges

persist, including the need to boost the ionic conductivity of solid electrolytes, improve interfacial stability, and refine manufacturing processes. Therefore, ongoing research is essential to develop high-performance solid electrolytes that are compatible with both PBA cathodes and Na metal anodes, which is crucial for achieving practical all-solid-state SIBs.

#### 6.5. Industrial Application

Although SIBs may not achieve the same high specific energy density as commercial LIBs, their cost benefits are strategically important, especially during times of Li resource shortages or price increases. SIBs act as a safeguard against supply chain vulnerabilities associated with LIBs and are particularly well-suited for applications where cost and cycle life are prioritized over energy density, such as grid-scale energy storage, electric bicycles, and portable electronics. PBAs are gaining distinct advantages in affordable large-scale energy storage due to their excellent compatibility with SIB systems. Current SIBs can reach energy densities of 100–150 Wh kg<sup>-1</sup>, which is a significant improvement over lead-acid batteries and competitive with some lithium iron phosphate (LFP) batteries. The European startup Altris has increased production of high-Na-content Fe-PBAs using a low-temperature, high-pressure synthesis method. Contemporary Amperex Technology Co. Limited (CATL) has developed first-generation PBA-based SIBs that provide 160 Wh kg<sup>-1</sup> at the full-cell level, featuring ultrafast charging (80% in 15 min at room temperature) and excellent low-temperature performance (90% capacity retention at -20 °C). Notably, this system shows over 2000-cycle stability, narrowing the performance gap with LIBs. The commercialization of these technologies is speeding up, with third-generation Fe-PBAs being developed to further improve energy density and safety for wider applications. With focused efforts in theoretical research, material development, and process refinement, the broad commercial use of PBAs in SIBs seems likely, marking a significant advancement in cost-effective, advanced energy storage solutions.

## Acknowledgements

This research was supported by the Nano and Material Technology Development Program through the National Research Foundation (NRF) of Korea funded by the Ministry of Science and ICT (RS-2024-00449682). The authors would like to acknowledge financial support from the Brazil government agencies including CNPq (Bolsa de Produtividade 307418/2021-9) and FAPERJ (E-26-210.965/2021, E-26-210.801/2021, and E-26-200.320/2023).

## Conflict of Interest

The authors declare no conflict of interest.

**Keywords:** modification strategies · Prussian blue analogs · sodium-ion batteries · synthesis techniques

- [1] W. Chen, Y. Hu, Y. P. Liu, S. Wang, A. Hu, T. Y. Lei, Y. Y. Li, P. Li, D. J. Chen, L. Xia, L. X. Xue, Y. C. Yan, G. X. Lu, M. J. Zhou, Y. X. Fan, H. Yang, X. Y. Tao, X. F. Wang, Y. R. Li, J. Xiong, *Adv. Mater.* **2024**, *36*, 2312880.
- [2] F. H. Li, Y. W. Li, K. S. Novoselov, F. Liang, J. Meng, S.-H. Ho, T. Zhao, H. Zhou, A. Ahmad, Y. Zhu, L. X. Hu, D. X. Ji, L. Jia, R. Liu, S. Ramakrishna, X. C. Zhang, *Nano-Micro Lett.* **2023**, *15*, 35.
- [3] Q. C. Zhu, D. Y. Zhao, M. Y. Cheng, J. Q. Zhou, K. A. Owusu, L. Mai, Y. Yu, *Adv. Energy Mater.* **2019**, *9*, 1901081.
- [4] S. Seenivasan, S. Adhikari, A. T. Sivagurunathan, D.-H. Kim, *Energy Environ. Sci.* **2025**, *18*, 1054.
- [5] Y. Chen, K. Fan, Y. Gao, C. L. Wang, *Adv. Mater.* **2022**, *34*, 2200662.
- [6] L. Ma, N. Li, S. Zhou, X. G. Zhang, K. Xie, *Adv. Energy Mater.* **2024**, *14*, 2401157.
- [7] Z. Z. Wang, J. F. Ni, L. Li, *ACS Energy Lett.* **2022**, *7*, 4106.
- [8] F. Li, M. Hou, L. Zhao, D. Zhang, B. Yang, F. Liang, *Energy Storage Mater.* **2024**, *65*, 103181.
- [9] W. R. Hou, X. W. Guo, X. Y. Shen, K. Amine, H. J. Yu, J. Lu, *Nano Energy* **2018**, *52*, 279.
- [10] L. L. Fan, Z. H. Li, N. P. Deng, *Energy Storage Mater.* **2021**, *41*, 152.
- [11] X. M. Liu, Z. Yang, Y. Lu, Z. L. Tao, J. Chen, *Small Methods* **2024**, *8*, 2300688.
- [12] C. L. Wei, L. W. Tan, Y. C. Zhang, Z. R. Wang, J. K. Feng, Y. Qian, *Energy Storage Mater.* **2022**, *52*, 299.
- [13] Q. Liu, Z. Hu, W. Li, C. Zou, H. Jin, S. Wang, S. L. Chou, S.-X. Dou, *Energy Environ. Sci.* **2021**, *14*, 158.
- [14] W. Zhang, J. Peng, W. Hua, Y. Liu, J. S. Wang, Y. Liang, W. H. Lai, Y. Jiang, Y. Huang, W. Zhang, H. Yang, Y. G. Yang, L. Li, Z. J. Liu, L. Wang, S.-L. Chou, *Adv. Energy Mater.* **2021**, *11*, 2100757.
- [15] C. Zhan, T. Wu, J. Lu, K. Amine, *Energy Environ. Sci.* **2018**, *11*, 243.
- [16] T. F. Liu, Y. Zhang, Z. Jiang, X. Q. Zeng, J. P. Ji, Z. Li, X. H. Gao, M. H. Sun, Z. Lin, M. Ling, J. C. Zheng, C. Liang, *Energy Environ. Sci.* **2019**, *12*, 1512.
- [17] M. H. Zhang, Y. Li, F. Wu, Y. Bai, C. Wu, *Nano Energy* **2021**, *82*, 105738.
- [18] W. C. Zhang, J. Lu, Z. P. Guo, *Mater. Today* **2021**, *50*, 400.
- [19] H. Yang, D. Wang, Y. Liu, Y. Liu, B. Zhong, Y. Song, Q. Q. Kong, Z. Wu, X. D. Guo, *Energy Environ. Sci.* **2024**, *17*, 1756.
- [20] D. Q. Chen, W. Zhang, K. Y. Luo, Y. Song, Y. Zhong, Y. X. Liu, G. Wang, B. Zhong, Z. G. Wu, X. D. Guo, *Energy Environ. Sci.* **2021**, *14*, 2244.
- [21] Y. Sun, S. H. Guo, H. S. Zhou, *Energy Environ. Sci.* **2019**, *12*, 825.
- [22] S. Fang, D. Bresser, S. Passerini, *Adv. Energy Mater.* **2020**, *10*, 1902485.
- [23] J. Xiao, Y. Xiao, J. Li, C. Gong, X. M. Nie, H. Gao, B. Sun, H. Liu, G. X. Wang, *SmartMat* **2023**, *4*, e1211.
- [24] L. T. Ma, H. Cui, S. M. Chen, X. L. Li, B. Dong, C. Zhi, *Nano Energy* **2021**, *81*, 105632.
- [25] Y. Xiao, J. Xiao, H. K. Zhao, J. Li, G. Zhang, D. Zhang, X. Guo, H. Gao, Y. Wang, J. Chen, G. X. Wang, H. Liu, *Small* **2024**, *20*, 2401957.
- [26] M. C. Guo, W. J. Li, W. Tang, C. B. Tang, B. Cao, X. S. He, C. Fan, *Energy Storage Mater.* **2025**, *74*, 103979.
- [27] J. H. Hu, Y. Hong, M. C. Guo, Y. Hu, W. Tang, S. Xu, S. Jia, B. S. Wei, S. Liu, C. Fan, Q. C. Zhang, *Energy Storage Mater.* **2023**, *56*, 267.
- [28] P. Barpanda, L. Lander, S. Nishimura, A. Yamada, *Adv. Energy Mater.* **2018**, *8*, 1703055.
- [29] H. J. Huang, X. W. Wu, Y. J. Gao, Z. Y. Li, W. Wang, W. S. Dong, Q. Y. Song, S. J. Gan, J. Zhang, Q. Yu, *Adv. Energy Mater.* **2024**, *14*, 2304251.
- [30] J. Xiao, H. Gao, Y. Xiao, S. Wang, C. Gong, Z. Huang, B. Sun, C. L. Dong, X. Guo, H. Liu, G. X. Wang, *Chem. Eng. J.* **2025**, *506*, 160010.
- [31] T. W. Kim, S. H. Ahn, Y.-Y. Song, B. J. Park, C. Lee, A. Choi, M.-H. Kim, D.-H. Seo, S.-K. Jung, H.-W. Lee, *Angew. Chem., Int. Ed.* **2023**, *62*, e202309852.
- [32] S. Qiu, Y. Xu, X. Y. Wu, X. L. Ji, *Electrochim. Energy Rev.* **2022**, *5*, 242.
- [33] Y. Yang, J. B. Zhou, L. Wang, Z. Jiao, M. Xiao, Q. Huang, M. M. Liu, Q. Shao, X. L. Sun, J. J. Zhang, *Nano Energy* **2022**, *99*, 107424.
- [34] B. F. Zhang, J. H. Zhang, Y. X. He, Y. Yu, K. Zhou, H. Wang, *J. Mater. Chem. A* **2025**, *13*, 18183.
- [35] J. F. Qian, C. Wu, Y. L. Cao, Z. F. Ma, Y. Huang, X. Ai, H. Yang, *Adv. Energy Mater.* **2018**, *8*, 1702619.
- [36] C. L. Zhang, Y. Xu, M. Zhou, L. Liang, H. Dong, M. H. Wu, Y. Yang, Y. Lei, *Adv. Funct. Mater.* **2017**, *27*, 1604307.
- [37] J. Peng, W. Zhang, Q. Liu, J. Wang, S. Chou, H. Liu, S. Dou, *Adv. Mater.* **2022**, *34*, 2108384.
- [38] M. T. Xia, X. Zhang, T. T. Liu, H. X. Yu, S. Chen, N. Peng, R. T. Zheng, J. D. Zhang, J. Shu, *Chem. Eng. J.* **2020**, *394*, 124923.
- [39] Z. X. Zhu, Y. Meng, Y. Yin, Z. C. Liu, T. Jiang, Q. Peng, T. Yin, M. Y. Li, W. Chen, *Energy Storage Mater.* **2021**, *42*, 464.
- [40] Q. C. Wang, J. Li, H. Jin, S. Xin, H. C. Gao, *InfoMat* **2022**, *4*, e12311.
- [41] A. Komenda, P. Piatek, *Renew. Sust. Energy Rev.* **2025**, *217*, 115677.
- [42] W. Shu, J. X. Li, G. Zhang, J. S. Meng, X. P. Wang, L. Q. Mai, *Nano-Micro Lett.* **2024**, *16*, 128.
- [43] G. Z. Yang, Z. H. Liang, Q. Li, Y. Li, F. Tian, C. X. Wang, *ACS Energy Lett.* **2023**, *8*, 4085.
- [44] J. Peng, J. Wang, H. C. Yi, W. J. Hu, Y. H. Yu, J. W. Yin, Y. Shen, Y. Liu, J. H. Luo, Y. Xu, P. Wei, Y. Li, Y. Jin, Y. Ding, L. Miao, J. J. Jiang, J. T. Han, Y. H. Huang, *Adv. Energy Mater.* **2018**, *8*, 1702856.
- [45] W. L. Shu, C. H. Han, X. P. Wang, *Adv. Funct. Mater.* **2024**, *34*, 2309636.
- [46] K. Du, Y. Liu, Y. Zhao, H. Li, H. X. Liu, C. H. Sun, M. S. Han, T. Ma, Y. X. Hu, *Adv. Mater.* **2024**, *36*, 2404172.
- [47] H. Zhang, Y. Gao, J. Peng, Y. Fan, L. F. Zhao, L. Li, Y. Xiao, W. K. Pang, J. Z. Wang, S.-L. Chou, *Angew. Chem., Int. Ed.* **2023**, *62*, e202303953.
- [48] B. X. Xie, B. Sun, T. Gao, Y. Ma, G. P. Yin, P. J. Zuo, *Coord. Chem. Rev.* **2022**, *460*, 214478.
- [49] G. Oh, J. H. Kim, S. Kansara, H. K. Kang, H.-G. Jung, Y.-K. Sun, J.-Y. Hwang, *J. Energy Chem.* **2024**, *93*, 627.
- [50] J. M. Ge, L. Fan, A. M. Rao, J. Zhou, B. Lu, *Nat. Sustain.* **2022**, *5*, 225.
- [51] F. Ma, Q. Li, T. Y. Wang, H. G. Zhang, G. Wu, *Sci. Bull.* **2017**, *62*, 358.
- [52] M. W. Jiang, Z. D. Hou, L. Ren, Y. Zhang, J.-G. Wang, *Energy Storage Mater.* **2022**, *50*, 618.
- [53] P. Hu, W. Peng, B. Wang, D. D. Xiao, U. Ahuja, J. Réthoré, K. E. Aifantis, *ACS Energy Lett.* **2020**, *5*, 100.
- [54] Y. Xu, J. Wan, L. Huang, M. Y. Ou, C. Y. Fan, P. Wei, J. Peng, Y. Liu, Y. G. Qiu, X. P. Sun, C. Fang, Q. Li, J. Han, Y. H. Huang, J. A. Alonso, Y. Zhao, *Adv. Energy Mater.* **2019**, *9*, 1803158.
- [55] Y. F. Luo, J. L. Shen, Y. Yao, J. Dai, F. X. Ling, L. Li, Y. Jiang, X. J. Wu, X. H. Rui, Y. Yu, *Adv. Mater.* **2024**, *36*, 2405458.
- [56] M. Du, P. B. Geng, C. X. Pei, X. Y. Jiang, Y. Y. Shan, W. H. Hu, L. Ni, H. Pang, *Angew. Chem., Int. Ed.* **2022**, *61*, e202209350.
- [57] Z. X. Jing, M. Mamoor, L. T. Kong, L. Wang, B. Wang, M. Chen, F. Wang, G. M. Qu, Y. Y. Kong, D. Wang, X. He, C. Wang, X. T. Zhang, Y. Zhang, G. Wang, L. Q. Xu, *Angew. Chem., Int. Ed.* **2025**, *64*, e202423356.
- [58] J. Zheng, G. Wang, K. Zhang, J. Zheng, W. Fu, C. Zhang, J. Liu, J. Y. Wang, J. W. Li, F. Cai, W. Huang, M. Zhang, Z. R. Shen, *Chem. Eng. J.* **2024**, *502*, 157785.
- [59] T. Z. Yang, D. Luo, X. Zhang, S. Gao, R. Gao, Q. Ma, H. W. Park, T. Or, Y. G. Zhang, Z. W. Chen, *Nat. Sustain.* **2024**, *7*, 776.
- [60] Y. Wang, Z. Sun, J. Zhu, F. Ye, J. Zhu, R. X. Li, G. T. Chang, *Colloids Surf. Physicochem. Eng. Asp.* **2025**, *716*, 136690.
- [61] T. X. Nguyen, J. Patra, K.-H. Yang, B. W. Saputro, O. Clemens, J.-K. Chang, J.-M. Ting, *J. Power Sources* **2024**, *624*, 235514.
- [62] X. Y. Wu, C. H. Wu, C. X. Wei, L. Hu, J. F. Qian, Y. L. Cao, X. P. Ai, J. Wang, H. Yang, *ACS Appl. Mater. Interfaces* **2016**, *8*, 5393.
- [63] L. X. Shen, Y. Jiang, Y. F. Liu, J. L. Ma, T. R. Sun, N. Zhu, *Chem. Eng. J.* **2020**, *388*, 124228.
- [64] M. S. Qin, W. H. Ren, R. X. Jiang, Q. Li, X. H. Yao, S. Wang, Y. You, L. Q. Mai, *ACS Appl. Mater. Interfaces* **2021**, *13*, 3999.
- [65] F. W. Peng, L. Yu, P. Y. Gao, X.-Z. Liao, J. Wen, Y.-S. He, G. Q. Tan, Y. Ren, Z. F. Ma, *J. Mater. Chem. A* **2019**, *7*, 22248.

- [66] Y. Shang, X. X. Li, J. J. Song, S. Z. Huang, Z. Yang, Z. J. Xu, H. Y. Yang, *Chem* **2020**, *6*, 1804.
- [67] Y. Wang, J. Liu, N. Jiang, J. H. Yang, C. Yang, Y. Liu, *Small* **2024**, *20*, 2403211.
- [68] M. W. Jiang, Z. Hou, J. Wang, L. Ren, Y. Zhang, J.-G. Wang, *Nano Energy* **2022**, *102*, 107708.
- [69] Y. You, X.-L. Wu, Y.-X. Yin, Y.-G. Guo, *Energy Environ. Sci.* **2014**, *7*, 1643.
- [70] L. Wang, J. Song, R. Qiao, L. A. Wray, M. A. Hossain, Y.-D. Chuang, W. Yang, Y. Lu, D. Evans, J.-J. Lee, S. Vail, X. Zhao, M. Nishijima, S. Kakimoto, J. B. Goodenough, *J. Am. Chem. Soc.* **2015**, *137*, 2548.
- [71] L.-P. Wang, P.-F. Wang, T.-S. Wang, Y.-X. Yin, Y.-G. Guo, C.-R. Wang, *J. Power Sources* **2017**, *355*, 18.
- [72] M. Hu, J.-S. Jiang, R.-P. Jia, Y. Zeng, *CrystEngComm* **2009**, *11*, 2257.
- [73] S. Kang, S. Im, Y. Jeon, *Bull. Korean Chem. Soc.* **2015**, *36*, 2387.
- [74] M. Cao, X. L. Wu, X. Y. He, C. W. Hu, *Chem. Commun.* **2005**, *17*, 2241.
- [75] S. Wang, M. S. Qin, M. Huang, X. Huang, Q. Li, Y. You, *ACS Appl. Energy Mater.* **2022**, *5*, 6927.
- [76] Q. H. Han, Z. H. Yang, Y. Hu, S. Gao, X. Liu, C. P. Wang, J. Han, *Chem. Eng. J.* **2024**, *493*, 152575.
- [77] G. X. Zhang, Y. Lu, Y. Yang, H. Yang, Z. Yang, S. X. Wang, W. T. Li, Y. Y. Sun, J. F. Huang, Y. S. Luo, H.-Y. Chen, Y.-F. Liao, H. Ishii, S. Gull, M. Shakouri, H.-G. Xue, Y. F. Hu, H. Pang, *J. Am. Chem. Soc.* **2024**, *146*, 16659.
- [78] Y. Gao, X. Y. Zhang, H. Zhang, J. Peng, W. Hua, Y. Xiao, X.-H. Liu, L. Li, Y. Qiao, J.-Z. Wang, C. F. Zhang, S. Chou, *Adv. Mater.* **2025**, *37*, 2409782.
- [79] W. Z. Gong, R. Zeng, S. Su, M. Wan, Z. X. Rao, L. H. Xue, W. X. Zhang, *J. Nanopart. Res.* **2019**, *21*, 274.
- [80] W. Tang, Y. Y. Xie, F. W. Peng, Y. Yang, F. Feng, X.-Z. Liao, Y.-S. He, Z.-F. Ma, Z. Chen, Y. Ren, *J. Electrochem. Soc.* **2018**, *165*, A3910.
- [81] S. He, J. M. Zhao, X. H. Rong, C. L. Xu, Q. Q. Zhang, X. Shen, X. G. Qi, Y. Li, X. Li, Y. S. Niu, X. W. Li, S. Han, L. Gu, H. Z. Liu, Y.-S. Hu, *Chem. Eng. J.* **2022**, *428*, 131083.
- [82] J. Peng, Y. Gao, H. Zhang, Z. G. Liu, W. Zhang, L. Li, Y. Qiao, W. S. Yang, J. Z. Wang, S. X. Dou, S. Chou, *Angew. Chem., Int. Ed.* **2022**, *61*, e202205867.
- [83] V. D. Neff, *J. Electrochem. Soc.* **1985**, *132*, 1382.
- [84] X. Y. Liu, Y. Cao, J. Sun, *Adv. Energy Mater.* **2022**, *12*, 2202532.
- [85] J. Liu, J. Liu, M. X. Tang, J. Fu, X. J. Kuang, J. Ma, *Adv. Funct. Mater.* **2024**, *34*, 2314167.
- [86] X. Liu, Y. Cao, J. Sun, *Adv. Energy Mater.* **2022**, *12*, 2202532.
- [87] Q. Guo, S. Han, Y. X. Lu, R. J. Xiao, J. Li, Q. Hao, X. H. Rong, S. Weng, Y. S. Niu, F. X. Ding, Y. Yang, H. Xia, X. F. Wang, F. Xie, L. Zhou, X. Hou, H. Li, X. J. Huang, L. Q. Chen, Y.-S. Hu, *Nat. Commun.* **2025**, *16*, 4707.
- [88] M. Pasta, R. Y. Wang, R. Ruffo, R. M. Qiao, H.-W. Lee, B. Shyam, M. H. Guo, Y. Wang, L. A. Wray, W. Yang, M. F. Toney, Y. Cui, *J. Mater. Chem. A* **2016**, *4*, 4211.
- [89] Z. H. Liang, F. Tian, G. Z. Yang, C. X. Wang, *Nat. Commun.* **2023**, *14*, 3591.
- [90] Y. Gao, H. Zhang, J. Peng, J. S. Wang, X. H. Liu, L. L. Zhang, Y. Xiao, L. Li, Y. Liu, Y. Qiao, J. Z. Wang, S. Chou, *Adv. Mater.* **2025**, 2417876, <https://doi.org/10.1002/adma.202417876>.
- [91] L. T. Kong, Z. X. Jing, M. Mamoor, Y. Jiang, Y. J. Zhai, G. M. Qu, L. Wang, B. Wang, L. Q. Xu, *Angew. Chem., Int. Ed.* **2025**, *64*, e202500254.
- [92] X. Zhao, Z. H. Xing, C. D. Huang, *J. Mater. Chem. A* **2023**, *11*, 22835.
- [93] J. Peng, B. Zhang, W. Hua, Y. Liang, W. Zhang, Y. M. Du, G. Peleckis, S. Idris, Q. Gu, Z. X. Cheng, J. Z. Wang, H. Liu, S. X. Dou, S. Chou, *Angew. Chem., Int. Ed.* **2023**, *62*, e202215865.
- [94] Z. Qian, R.-J. Luo, C. Ma, C.-Y. Du, J. Zeng, X. Xu, Z. Mei, Z.-T. Zhou, Z.-W. Fu, Y.-N. Zhou, *Chem. Eng. J.* **2024**, *500*, 156767.
- [95] J. Dai, S. Tan, L. F. Wang, F. X. Ling, F. Q. Duan, M. Z. Ma, Y. Shao, X. H. Rui, Y. Yao, E. Y. Hu, X. J. Wu, C. Y. Li, Y. Yu, *ACS Nano* **2023**, *17*, 20949.
- [96] Y. Y. He, S. L. Dreyer, Y.-Y. Ting, Y. Ma, Y. Hu, D. Goonetilleke, Y. Tang, T. Diemant, B. Zhou, P. M. Kowalski, M. Fichtner, H. Hahn, J. A. Hagmann, T. Brezesinski, B. Breitung, Y. J. Ma, *Angew. Chem., Int. Ed.* **2024**, *63*, e202315371.
- [97] L. Wang, Y. Lu, J. Liu, M. W. Xu, J. G. Cheng, D. Zhang, J. B. Goodenough, *Angew. Chem., Int. Ed.* **2013**, *52*, 1964.
- [98] H.-W. Lee, R.-Y. Wang, M. Pasta, S. W. Lee, N. Liu, Y. Cui, *Nat. Commun.* **2014**, *5*, 5280.
- [99] C. Li, R. Zang, P. X. Li, Z. M. Man, S. Wang, X. M. Li, Y. H. Wu, S. S. Liu, G. X. Wang, *Chem. Asian J.* **2018**, *13*, 342.
- [100] X. Liu, H. C. Gong, C. Y. Han, Y. Cao, Y. T. Li, J. Sun, *Energy Storage Mater.* **2023**, *57*, 118.
- [101] C. Wei, X.-Y. Fu, L.-L. Zhang, J. Liu, P.-P. Sun, L. Gao, K.-J. Chang, X.-L. Yang, *Chem. Eng. J.* **2021**, *421*, 127760.
- [102] Z. Xu, F. Q. Chen, Y. Li, Y. H. Lu, A. Zhou, J. C. Jiang, X. W. Xu, J. Tu, B. Pan, F. Chen, Y. Huang, X. B. Zhao, J. Xie, *Adv. Sci.* **2024**, *11*, 2406842.
- [103] X. Y. Zhao, N. Liu, M. X. Zheng, X. H. Wang, Y. Xu, J. W. Liu, F. Li, L. B. Wang, *ACS Energy Lett.* **2024**, *9*, 2748.
- [104] M. H. Ye, S. Z. You, J. M. Xiong, Y. Yang, Y. F. Zhang, C. C. Li, *Mater. Today Energy* **2022**, *23*, 100898.
- [105] Z.-Y. Chen, L.-L. Zhang, X.-Y. Fu, B. Yan, X.-L. Yang, *ACS Appl. Mater. Interfaces* **2022**, *14*, 43308.
- [106] J. Peng, Y. Liao, Y. Zhang, K. Huang, Y. Han, W. Chen, L. H. Xue, W. X. Zhang, *ACS Appl. Nano Mater.* **2023**, *7*, 27822.
- [107] D. S. Kim, H. D. Yoo, M.-S. Park, H. Kim, *J. Alloys Compd.* **2019**, *791*, 385.
- [108] Q. Xue, L. Li, Y. X. Huang, R. L. Huang, F. Wu, R. J. Chen, *ACS Appl. Mater. Interfaces* **2019**, *11*, 22339.
- [109] K.-R. Ren, J.-C. Wang, S.-H. Tian, N. Ren, P.-F. Wang, T.-F. Yi, *Mater. Res. Bull.* **2023**, *166*, 112351.
- [110] X. Y. Fu, L. L. Zhang, Z. Y. Chen, Y. K. Xu, J. X. Wu, C. C. Wang, X. K. Ding, X. L. Yang, J. Lu, *Carbon Energy* **2024**, *6*, e446.
- [111] M. M. Giner, R. S. Gual, J. Romero, A. Alberola, L. G. Cruz, S. Agouram, M. Galbiati, N. M. Padial, J. C. Waerenborgh, C. M. Gastaldo, S. Tatay, A. F. Aliaga, E. Coronado, *Adv. Funct. Mater.* **2018**, *28*, 1706125.
- [112] Y. Qiao, G. Wei, J. B. Cui, M. M. Zhang, X. G. Cheng, D. He, S. Li, Y. Liu, *Chem. Commun.* **2019**, *55*, 549.
- [113] F. W. Peng, L. Yu, S. Yuan, X. Z. Liao, J. G. Wen, G. Q. Tan, F. Feng, Z. F. Ma, *ACS Appl. Mater. Interfaces* **2019**, *11*, 37685.
- [114] C. L. Xu, Y. Z. Ma, J. M. Zhao, P. Zhang, Z. Chen, C. Yang, H. Z. Liu, Y. S. Hu, *Angew. Chem., Int. Ed.* **2023**, *62*, e202217761.
- [115] N. Kitchamsetti, J. Cho, C. S. Chakra, *Chem. Eng. J.* **2024**, *495*, 153353.
- [116] Y. M. Liu, Y. Q. Gong, K. Chen, L. J. Zhu, Y. An, K. I. Ozoemena, W. Hua, M. H. Yang, Q. Q. Pang, *Adv. Funct. Mater.* **2024**, *34*, 2403138.
- [117] Y. F. Huang, H. Yan, W. B. Liu, F. Y. Kang, *Angew. Chem., Int. Ed.* **2024**, *63*, e202409642.
- [118] Y. X. J. Wang, Z. Y. Zhang, K. Tang, Y. C. Li, G. H. Li, J. Wang, Z. J. Wu, N. Zhang, X. Q. Xie, *J. Energy Chem.* **2025**, *107*, 241.
- [119] J. Zhang, J. W. Li, G. F. Jia, H. Y. Wang, M. Wang, *J. Energy Chem.* **2025**, *102*, 340.
- [120] Q. Liu, Y. H. Feng, X. Zhu, M. T. Liu, L. Z. Yu, G. X. Wei, X. Y. Fan, X. Ji, P. F. Wang, H. S. Xin, *Nano Energy* **2024**, *123*, 109389.
- [121] B. X. Xie, P. J. Zuo, L. G. Wang, J. J. Wang, H. Huo, M. X. He, J. Shu, H. F. Li, S. F. Lou, G. P. Yin, *Nano Energy* **2019**, *61*, 201.
- [122] B. X. Xie, L. G. Wang, H. F. Li, H. Huo, C. Cui, B. Y. Sun, Y. Ma, J. J. Wang, G. P. Yin, P. J. Zuo, *Energy Storage Mater.* **2021**, *36*, 99.
- [123] K. Luo, Z. X. Wang, Y. Mo, J. L. Ke, W. Zhou, K. X. Wang, S. Chen, P. Gao, A. Hu, J. Liu, *Adv. Funct. Mater.* **2024**, *34*, 2311364.
- [124] X. X. Jian, X. W. Liu, C. Yang, J. Xie, W. X. Hu, Y. C. Zhang, H. Yan, J. Han, Y. You, *Small* **2024**, *20*, 2400709.
- [125] B. X. Xie, Y. Du, Y. Ma, S. S. Liu, Y. Wang, P. J. Zuo, Y. Z. Gao, G. P. Yin, *ACS Sustainable Chem. Eng.* **2021**, *9*, 5809.
- [126] X. H. Liu, J. H. Zhao, H. H. Dong, L. L. Zhang, H. Zhang, Y. Gao, X. Z. Zhou, L. H. Zhang, L. Li, Y. Liu, S. C. Chou, W. H. Lai, C. F. Zhang, S. Chou, *Adv. Funct. Mater.* **2024**, *34*, 2402310.
- [127] H. Liu, X. X. Liu, W. Li, X. Guo, Y. Wang, G. X. Wang, D. Y. Zhao, *Adv. Energy Mater.* **2017**, *7*, 1700283.
- [128] T. Y. Lyu, F. Q. Luo, D. C. Wang, L. Z. Bu, L. Tao, Z. F. Zheng, *Adv. Energy Mater.* **2022**, *12*, 2201493.
- [129] Y. C. Hu, J. K. Yang, J. P. Hu, J. X. Wang, S. Liang, H. J. Hou, X. Wu, B. C. Liu, W. H. Yu, X. He, R. V. Kumar, *Adv. Funct. Mater.* **2018**, *28*, 1705294.
- [130] L. Yang, S. Li, Y. Zhang, H. Feng, J. P. Li, X. Y. Zhang, H. Guan, L. Kong, Z. H. Chen, *J. Energy Chem.* **2024**, *97*, 30.
- [131] Y. Z. Jiang, S. L. Yu, B. Wang, Y. Li, W. P. Sun, Y. H. Lu, M. Yan, B. Song, S. X. Dou, *Adv. Funct. Mater.* **2016**, *26*, 5315.
- [132] Y. C. Wang, N. Jiang, C. Yang, J. Liu, S. Sun, X. Wang, J. H. Yang, Y. Liu, *J. Mater. Chem. A* **2024**, *12*, 5170.
- [133] J. Lee, W. C. Jeong, J. Baek, Y. M. Kim, Y. Choi, V. Mathew, B. Sambandam, M. H. Alfaruqi, J. Kim, *J. Mater. Chem. A* **2023**, *11*, 25724.
- [134] S. P. Zhang, G. Wang, B. B. Wang, J. Wang, J. Bai, H. Wang, *Adv. Funct. Mater.* **2020**, *30*, 2001592.
- [135] J. Zhang, J. Zhang, H. H. Wang, V. W. Lau, G. H. Lee, K. Zhang, M. Park, Y. M. Kang, *ACS Energy Lett.* **2022**, *7*, 4472.
- [136] Y. Tang, L. Wang, J. W. Hu, M. Chen, M. Zhou, K. Wang, K. Jiang, *Adv. Energy Mater.* **2024**, *14*, 2303015.
- [137] M. W. Jiang, Z. D. Hou, H. H. Ma, J. J. Wang, W. Hua, L. B. Ren, Y. Zhang, C. G. Wei, F. Kang, J. G. Wang, *Nano Lett.* **2023**, *23*, 10423.
- [138] Y. X. Huang, M. Xie, Z. H. Wang, Y. Jiang, Y. Yao, S. Li, Z. Li, L. Li, F. Wu, R. Chen, *Small* **2018**, *14*, 1801246.

- [139] F. Gebert, D. L. Cortie, J. C. Bouwer, W. Wang, Z. C. Yan, S. X. Dou, S. L. Chou, *Angew. Chem., Int. Ed.* **2021**, *60*, 18519.
- [140] F. Feng, S. Chen, S. Q. Zhao, W. Zhang, Y. G. Miao, H. Y. Che, X. Z. Liao, Z. F. Ma, *Chem. Eng. J.* **2021**, *411*, 128518.
- [141] Z. T. Pan, Z. H. He, J. F. Hou, L. B. Kong, *Small* **2023**, *19*, 2302788.
- [142] T. U. Choi, G. G. Baek, S. G. Lee, J. H. Lee, *ACS Appl. Mater. Interfaces* **2020**, *12*, 24817.
- [143] D. X. Zuo, C. P. Wang, J. J. Han, Q. H. Han, Y. Hu, J. W. Wu, H. Qiu, Q. Zhang, X. J. Liu, *J. Mater. Sci. Technol.* **2022**, *114*, 180.
- [144] X. Hu, W. S. Jian, N. Y. Hong, X. Zhong, M. Yang, S. S. Tao, J. Huang, H. Wang, J. Q. Gao, W. T. Deng, G. Q. Zou, H. S. Hou, D. S. Silvester, C. E. Banks, X. Ji, *Angew. Chem., Int. Ed.* **2024**, *63*, e202410420.
- [145] G. He, L. F. Nazar, *ACS Energy Lett.* **2017**, *2*, 1122.
- [146] S. W. Fan, Y. L. Y.Gao, L. Li, L. L. Zhang, Z. M. Zhou, S. L. Chou, X. T. Liu, Y. Shen, Y. H. Huang, Y. Qiao, *ACS Energy Lett.* **2025**, *10*, 1751.
- [147] J. W. Nai, J. T. Zhang, X. W. Lou, *Chem* **2018**, *4*, 1967.
- [148] P. Wan, H. Xie, N. Zhang, S. Zhu, C. Wang, Z. Yu, W. S. Chu, L. Song, S. Q. Wei, *Adv. Funct. Mater.* **2020**, *30*, 2002624.
- [149] W. Zhang, Y. Zhao, V. Malgras, Q. M. Ji, D. M. Jiang, R. J. Qi, K. Ariga, Y. Yamauchi, J. Liu, J. S. Jiang, M. Hu, *Angew. Chem., Int. Ed.* **2016**, *55*, 8228.
- [150] X. H. Liu, W. H. Lai, S. L. Chou, *Mater. Chem. Front.* **2020**, *4*, 1289.
- [151] M. S. Qin, W. H. Ren, J. S. Meng, X. P. Wang, X. H. Yao, Y. Ke, Q. Li, L. Q. Mai, *ACS Sustainable Chem. Eng.* **2019**, *7*, 11564.
- [152] W. H. Ren, M. S. Qin, Z. X. Zhu, M. Y. Yan, Q. Li, L. Zhang, D. Liu, L. Q. Mai, *Nano Lett.* **2017**, *17*, 4713.
- [153] D. X. Zuo, C. P. Wang, J. J. Han, J. W. Wu, H. J. Qiu, Q. Zhang, Y. Lu, Y. J. Lin, X. J. Liu, *ACS Sustainable Chem. Eng.* **2020**, *8*, 16229.
- [154] R. Wei, X. Zhai, H. R. Tinker, P. He, C. A. F. Nason, Y. Han, V. Celorrio, G. Sankar, M. Zhou, Y. Xu, *Adv. Funct. Mater.* **2023**, *33*, 2308227.
- [155] A. Simonov, T. D. Baerdemaeker, H. L. B. Boström, M. L. R. Gómez, H. J. Gray, D. Chernyshov, A. Bosak, H. B. Bürgi, A. L. Goodwin, *Nature* **2020**, *578*, 256.
- [156] C. W. Gao, M. Chen, J. T. Li, X. Wang, G. B. Zhang, X. Tan, S. H. Zhang, G. Feng, D. Y. Zhai, F. Kang, *Energy Environ. Sci.* **2024**, *17*, 9278.
- [157] J. Y. Yang, G. H. Mao, T. Y. Yao, L. Shen, Y. Yu, *Angew. Chem., Int. Ed.* **2025**, *64*, e202420413.
- [158] L. Ge, Y. Song, P. C. Niu, B. Y. Li, L. Zhou, W. T. Feng, C. X. Ma, X. J. Li, D. Kong, Z. F. Yan, Q. Z. Xue, Y. P. Cui, W. Xing, *ACS Nano* **2024**, *18*, 3542.
- [159] J. Ning, J. W. Hu, M. Zhou, T. Wang, M. Chen, K. Wang, W. Wang, K. Jiang, *Chem. Eng. J.* **2024**, *489*, 151531.
- [160] J. Hu, H. Tao, M. Chen, Z. Zhang, S. Cao, Y. Shen, K. Jiang, M. Zhou, *ACS Appl. Mater. Interfaces* **2022**, *14*, 12234.
- [161] X. Xu, S. Zhu, C. Yang, Y. D. Wang, Z. Wu, J. Zheng, J. Wu, Y. F. Gao, *J. Mater. Chem. A* **2025**, *13*, 11848.
- [162] G. Y. Du, M. Tao, J. Li, T. T. Yang, W. Gao, J. H. Deng, Y. R. Qi, S. J. Bao, M. W. Xu, *Adv. Energy Mater.* **2020**, *10*, 190351.
- [163] R. Z. Wei, X. W. Zhai, H. R. Tinker, P. He, C. A. F. Nason, Y. P. Han, V. Celorrio, G. Sankar, M. Zhou, Y. Xu, *Adv. Funct. Mater.* **2023**, *33*, 2308227.
- [164] S. Qiao, S. Dong, L. L. Yuan, T. Li, M. Ma, Y. Wu, Y. Z. Hu, T. Qu, S. Chong, *J. Alloys Compd.* **2023**, *950*, 169903.
- [165] H. Cheng, Y. Qin, Y. N. Liu, Z. E. Yu, R. Li, R. Chen, J. Zhou, Y. Liu, B. K. Guo, *J. Mater. Chem. C* **2024**, *12*, 6785.
- [166] C. Zhao, Z. Yao, D. Zhou, L. Jiang, J. Wang, V. Murzin, Y. Lu, X. Bai, A. A. Guzik, L. Chen, Y. S. Hu, *Adv. Funct. Mater.* **2020**, *30*, 1910840.
- [167] Y. Chen, Y. Shi, J. X. Chen, H. Liu, X. Pan, Y. Jin, J. Chen, *J. Power Sources* **2024**, *615*, 235085.
- [168] K. Wang, M. X. Yang, Q. Liu, S. Cao, Y. Wang, T. Hu, Z. Peng, *J. Colloid Interface Sci.* **2025**, *678*, 346.
- [169] Y. Huang, M. Xie, Z. Wang, Y. Jiang, Y. Yao, S. Li, Z. Li, L. Li, F. Wu, R. Chen, *Small* **2018**, *14*, 1801246.

Manuscript received: June 25, 2025

Revised manuscript received: July 29, 2025

Version of record online: